Insurance Institute for Business & Home Safety

Where building science leads to real-world solutions.



2013 IBHS Characteristics of Severe Hail Field Research Summary

Ian M. Giammanco, PhD

Research Scientist

Tanya M. Brown, PhD

South Carolina Wind and Hail Underwriting Association Research Engineer

Insurance Institute for Business & Home Safety

February 25, 2014

IBHS – RC02 – 2014

Table of Contents

Table of Contents 2
List of Figures 3
List of Tables 4
Abbreviations 5
Acknowledgements 6
Abstract 7
1 Introduction 8
2 Objectives 8
3 Field Project Instrumentation 9
4 Data Collection Methods 11
5 Dataset Summary 13
5.1 Mission #1 13
5.1.1 Case Studies 18
5.1.1.1 Case Study 1: May 19 in Wichita, Kansas 19
5.1.1.2 Case Study 2: May 20 in Antioch/Maysville, Oklahoma 21
5.2 Mission #2 26
6 Application of Field Observations in Laboratory Testing 30
6.1 Mass and Diameter 30
6.2 Kinetic Energy 32
6.3 Compressive Stress 36
7 Summary 38
8 References 40

List of Figures

Figure 1: Photograph of a compressive force device used during the 2013 field study. 10
Figure 2: A photograph of the IBHS Camera Probe in its deployment configuration. 11
Figure 3: A photograph of the largest hailstone measured by IBHS field teams. 12
Figure 4: Diagram of the measured dimensions of hailstones. 13
Figure 5: A map of Mission #1 deployment locations 14
Figure 6: Compressive stress shown as a function of the x_1 dimension. 17
Figure 7: Same as Figure 6 except compressive stress is shown as a function of mass. 17
Figure 8: Compressive force at fracture (non-scaled) shown as a function of mass 18
Figure 9: Radar 0.5 degree reflectivity from the KICT WSR-88D radar at 2036 UTC on May 19, 2013 19
Figure 10: Measured peak (blue), mean (red) hail size (top) and compressive force (middle) at each deployment location compared with the WDSSII MESH hail swath (bottom). 21
Figure 11: Radar 0.5 degree reflectivity from the KTLX WSR-88D at 2133 UTC on May 20, 2013. 22
Figure 12: Measured peak (blue), mean (red) hail size (top-left), and compressive stress (top-right) at each deployment location compared with the WDSSII MESH hail swath (bottom) 23
Figure 13: Image from camera #3 at 2109 UTC and associated KTLX radar reflectivity at 2107 on May 20, 2013. 24
Figure 14: Estimated timeline of the evolution of the precipitation pattern derived from subjective analysis of imagery collected by the Camera Probe from 2037 UTC through 2145 UTC on May 20, 2013. 25
Figure 15: Map of Mission #2 deployments. 27
Figure 16: Compressive stress shown as a function of the measured x_1 dimension. 29
Figure 17: Same as Figure 16 expect shown as a function of mass. 29
Figure 18: Compressive force at fracture (non-scaled) shown as a function of the measured mass. 30
Figure 19: Comparison of mass-diameter relationship for field and laboratory hailstones 31
Figure 20: Schematic of differences in dimensions and associated volumes for spheres vs. disc-shaped spheroids 32
Figure 21: Estimated impact kinetic energy for a horizontal wind speed of 10 mph shown as a function of diameter for measured natural hailstones (2012 and 2013), compared to (A) UL 2218 (2012) steel ball material performance ratings and (B) FM 4473 (2005) ice ball material performance ratings.. 34
Figure 22: Same as Figure 21 but for a uniform horizontal wind of 60 mph. 35
Figure 23: Comparison of field and laboratory compressive force values as a function of the measured x_1 dimension. 37
Figure 24: Comparison of the ranges and mean compressive stress data for the combined 2012 and 2013 field data and the various laboratory experimental data. 38

List of Tables

Table 1: 2013 Mission #1 teams 14
Table 2: 2013 Mission #1 summary data 15
Table 3: 2013 Mission #2 teams 26
Table 4: 2013 Mission #2 summary data 28

Abbreviations

IBHS: Insurance Institute for Business & Home Safety
MESH: Maximum Expected Size of Hail
NSSL: National Severe Storms Laboratory
NWS: National Weather Service
UL: Underwriters Laboratory
WDSSII: Warning Decision Support System of Integrated Information
WSR-88D: Weather Surveillance Radar-1988 Doppler

Acknowledgements

The authors wish to acknowledge staff from State Farm Insurance's Technology Research and Innovation Laboratory (TRAIL) and the Enterprise Public Affairs Digital Media Team for participating during Mission #1. This valuable partnership allowed two measurement teams to collect very high spatial resolution data across the hail swath and publicize the project through social media outreach. Additionally, IBHS again partnered with WeatherPredict Consulting Inc., an affiliate of RenaissanceRe. WeatherPredict supported the IBHS project by archiving computer model initialization data for each operation day during both the 2012 and 2013 field phases.

Abstract

In 2012, the Insurance Institute for Business & Home Safety (IBHS) began a long-term hail field research program in an effort to characterize damaging hail which depends on size, density, and hardness of hailstones. The field study conducted during the late spring of 2012 provided the first in-situ measurements of the hardness property of hailstones, which was quantified using a custom instrumentation platform. Efforts to expand upon the database of hailstones measured were continued in 2013, to improve the spatial resolution of measurements, and to obtain more data on larger stones. In 2013, data on 685 stones from 12 parent thunderstorms were collected. Several high spatial resolution cases were collected with approximately 1 to 2 mile spacing between data collection points across the width of the hail swath, and two of these cases are described in detail. Comparisons of laboratory and field hailstone measurements are discussed. A new instrumentation platform, the IBHS photogrammetric Camera Probe, was also introduced, and enabled investigations into the frequency and spatial distributions of hailfall at a particular location. The imagery collected by the Camera Probe proved useful in determining the timing of hailfall when to the radar indications.

1 Introduction

In 2012, the Insurance Institute for Business & Home Safety (IBHS) began a long-term hail field research program to characterize damaging hail which depends on size, density, and hardness of hailstones. The field study conducted during the late spring of 2012 provided the first in-situ measurements of the hardness property of hailstones. This is quantified using a custom instrumentation platform which measures the compressive force required to fracture a hailstone. In 2012, 239 individual hailstones were sampled from nine parent thunderstorms. The sizes of the hailstones ranged from 0.16 in. to 3.05 in., and compressive stress values ranged from 9 psi to 628 psi (Giammanco and Brown, 2013). In 2013, the project continued to expand upon the database of hailstones measured, to improve the spatial resolution of measurements, and to obtain more data on larger stones. A new instrumentation platform, the IBHS photogrammetric Camera Probe, also was introduced.

The observations collected during the 2012 and 2013 hail field studies continue to guide the production of experimental laboratory hailstones at the IBHS Research Center, and allow for investigation of the modes and severity of damage caused by impacts of hailstones with varying size, density, and hardness. These data also are used to investigate the relationships between the type of hailstones produced and the large- and storm-scale environments. The 2012 dataset exhibited some evidence that a relationship between the parent thunderstorm and the mean hailstone characteristics exists, and this will be investigated further as the 2013 dataset is assimilated. Additionally, the database will serve as validation data to researchers working on establishing improved hail detection algorithms for the newly-upgraded dual-polarization National Weather Service (NWS) Weather Surveillance Radar-1988 Doppler (WSR-88D) radars (Kumjian personal communication). The IBHS Camera Probe imagery also will be used to investigate the frequency and spatial coverage of hailstones falling at a single point. These data can be used to inform the large test chamber research, by providing validation for the propulsion frequencies of the hail cannons, which are electronically controlled and fully configurable. The current propulsion frequencies were determined subjectively through purely qualitative observations.

The 2013 study was led again by IBHS Research Scientist Dr. Ian Giammanco, a meteorologist who served as field coordinator for the project, and IBHS Research Engineer Dr. Tanya Brown, a meteorologist who served as logistics coordinator. The area of focus was the Great Plains region of the U.S., where severe hailstorms most commonly occur. The 2013 study featured two separate missions.

2 Objectives

The data collected in both the 2012 and 2013 hail field projects are used to guide ongoing research on evaluating current impact testing standards by using more realistic artificial hailstones rather than steel (Underwriter's Laboratory, 2012) or pure ice balls (FM Approvals, 2005, 2010). While the current tests produce valuable measures of the relative resistance of different products to impact damage, the steel or pure ice balls are not necessarily representative of the damaging hail produced in nature. It is

understood that a more massive stone will impart a larger force on any material it impacts. However, the effect of the hardness property of a given stone is not well understood. IBHS researchers hypothesize that hailstone hardness has a direct bearing on damage caused by hailstones impacts; specifically, while harder hailstones may be more likely to shatter brittle materials and crack the substrate of shingles, softer stones may cause less severe structural damage but create cosmetic damage that still leads to roofing replacement.

Specific objectives of the field study included:

- quantifying natural hailstone hardness, by evaluating the compressive force required to fracture a hailstone;
- improving upon data collection strategies by collecting high spatial resolution data across the hail swath for comparison with modeled or radar-indicated hail swaths;
- pilot-testing the newly-developed IBHS Camera Probe to examine local hailfall frequency and temporal variability
- examining radar and environmental data to develop relationships between those data fields and the characteristics of fallen hailstones.

3 Field Project Instrumentation

Before the 2012 study, IBHS staff developed a rugged instrument to measure the hardness properties of real hailstones. The custom-designed instrument features a clamping handle in which the force applied to a hailstone can be incrementally increased until it fractures. A strain-gauge load cell attached to the bottom plate of the device measures the force applied to the hailstone at extremely high sampling rates (e.g. 100 Hz) (Giammanco and Brown, 2013; Brown et al., 2012). This instrument was modified slightly to improve performance for the 2013 project, by replacing the original rectangular plate which contacted the top of each stone with a Delrin disk identical to the plate used to cradle each stone. A photograph of the two hardness instruments used in the 2013 field study is shown in Figure 1. A digital scale, caliper, and GPS camera also were used. Additionally, a mat with a ruler was used to photograph each stone to give a visual representation of the hailstone sizes. The software which interfaces with the compressive force instrument was updated to improve functionality and was used to record the mass and dimension data, as well as GPS location. The graphical user interface (GUI) was modified to provide a more user-friendly interface. Additional data functionality was also included to allow information to be archived in the event a compressive force test could not be made on a given stone (i.e. slushy, spongy, or measurement error) in order to preserve the dimension and mass measurements which are quite useful despite the absence of compressive force information.

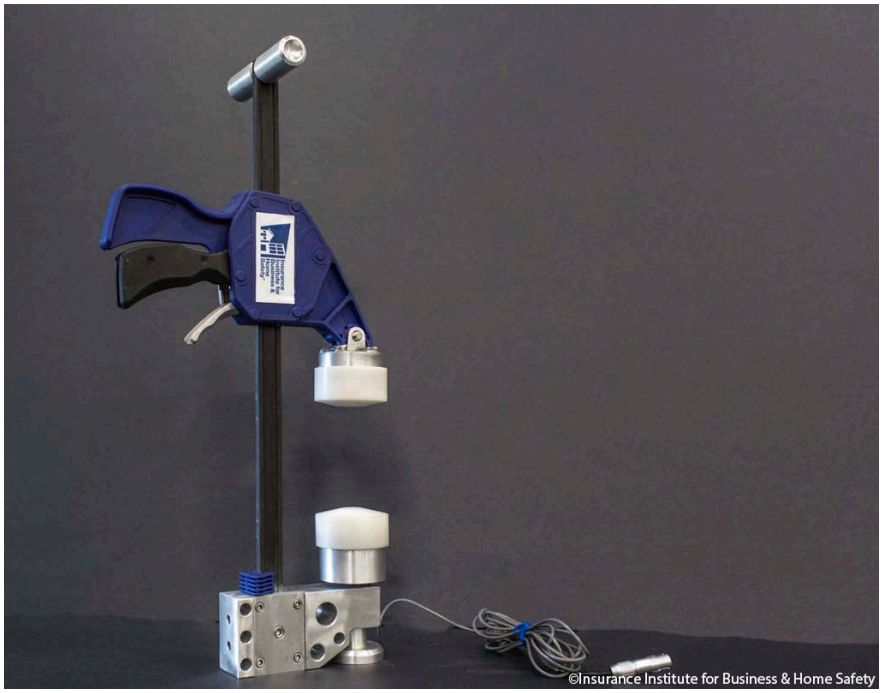


Figure 1: Photograph of a compressive force device used during the 2013 field study.

In addition to the two compressive force instruments, IBHS staff developed a ruggedized rapidly-deployable photogrammetric Camera Probe. The instrument featured three Go-Pro high-definition cameras arranged within a protected clear Lexan dome to capture a nearly-360^{o} field of view for run times of approximately 30 to 45 minutes. The unmanned probe was designed to be deployed in the path of the hail core of a thunderstorm, prior to the storm crossing the selected deployment road, allowing the deployment team to retreat away safely from the region of hailfall. Imagery from the probe was intended to capture qualitative information regarding the quantity and temporal patterns of hailfall. Through photogrammetric analyses, trajectories also could be estimated to evaluate the presence of wind-driven hail in various storm-relative locations. Figure 2 depicts the IBHS Camera Probe in its deployed form. The Camera Probe's support legs were designed not only to be collapsible and folded to limit their shipping and packaging size, but also to allow them to extend to improve the cameras' viewpoint height.



Figure 2: A photograph of the IBHS Camera Probe in its deployment configuration.

4 Data Collection Methods

Project coordinators used long-range numerical weather prediction models to determine several consecutive days in which conditions would support hail-producing thunderstorms in the Great Plains. Once deployed to the field, short-term forecasting and "now-casting" expertise was applied to determine daily locations where severe thunderstorms were likely to develop. When thunderstorm development began each day, the field coordinator identified a potential target storm and determined its likelihood of producing severe hail by evaluating radar data in near real-time. Given enough lead-time to ensure a safe deployment, the field coordinator directed the Camera Probe Team to a location most likely to be in the path of the hail core of the target thunderstorm. After deploying the probe, the Camera Probe Team then retreated and all teams then would position themselves safely near the target storm, but outside of the hailfall region, to wait until it passed.

After the passage of the target storm, the measurement teams transected the radar-estimated hail swath to identify where hail actually had fallen. If hailstones were large enough to measure, approximately 0.5 in. or larger, the teams selected deployment sites and began data collection. If not, they moved further into the hail swath in search of larger stones. At each deployment site, teams sought to obtain a representative sample, by collecting hailstones of all sizes, not just the largest ones. Each

stone was photographically cataloged, measured, weighed, and fractured with the compressive force instrument. An example of a photograph catalogued is provided in Figure 3, which is the largest stone collected in the two-year history of the project. A schematic of the dimensions measured is provided in Figure 4. The purpose of the dimension and mass measurements and their use in normalization techniques are described by Giammanco and Brown (2013) and Brown et al. (2012). In some cases, the hailstones were photographed, measured, and weighed, but the compressive force data could not be collected due to software or hardware difficulties, or if the stone was too spongy and just compressed without fracturing. Compressive force data were not collected for 6% of the 2013 dataset. These stones were removed from the compressive stress analyses, but the raw data were retained since the mass and dimension data are still quite valuable.

During measurements, members of the Camera Probe Team documented the measurement process with photographs and videos, before returning to collect the Camera Probe. The Camera Probe Team provided live updates on the teams' progress and status throughout the project using social media. In addition, the Camera Probe Team captured photographs and video footage for future use.



Figure 3: A photograph of the largest hailstone measured by IBHS field teams. This stone was collected on May 30, 2013 near Ratliff City, OK.

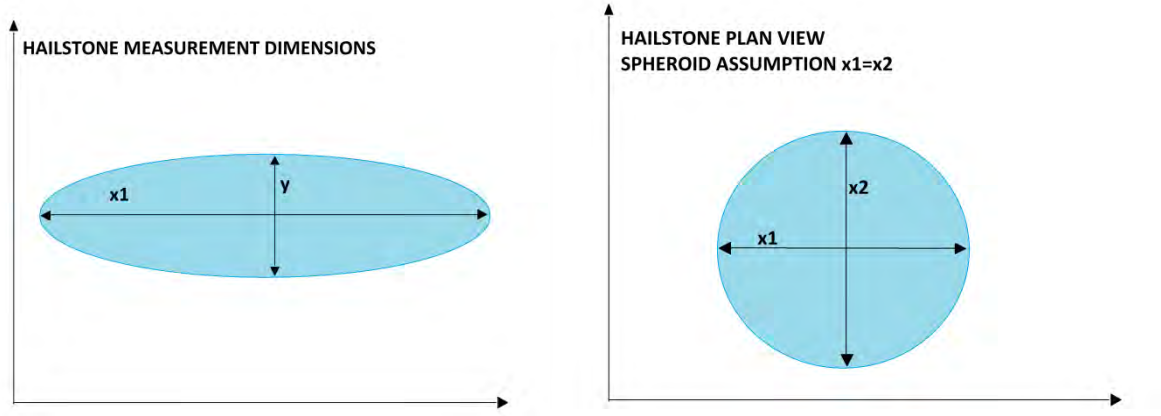


Figure 4: Diagram of the measured dimensions of hailstones. Each stone is assumed to be a spheroid with dimensions x_1 and x_2 equal. Dimensions x_1 and y were measured by field teams.

5 Dataset Summary

5.1 Mission #1

The first mission of the 2013 project began on May 16, when three teams arrived in Oklahoma City, Oklahoma. Mission #1 teams listed in Table 1 included representatives from IBHS member, State Farm Insurance Companies, and IBHS staff. The two members of State Farm's Technology Research and Innovation Laboratory (TRAIL) and the member of its Enterprise Public Affairs Digital Media Team (SF) are identified in Table 1. During Mission #1, teams traveled within Kansas, Nebraska, Oklahoma, and Texas, and successfully collected 33 datasets on hailstones from seven parent thunderstorms on four operations days, as shown in Figure 5. Table 2 provides summary statistics from Mission #1. The majority of hailstones measured were less than 1 in. in diameter, but at least one stone measured from each storm was larger than the severe criteria of 1 in., with the exception of storm 3D. The compressive force required to fracture each hailstone was scaled by the estimated cross-sectional area ($\pi x_1 y$) of the stone perpendicular to the compressive force, calculated from the dimension measurements. This normalization technique gives the resulting compressive stress at fracture in pounds/inch^2 (psi). As shown in Figure 6, this normalization technique results in a range of values of 1 psi to more than 670 psi. Additionally, Figure 7 presents the compressive stress at fracture as compared to the mass of the stone, while Figure 8 presents the compressive force at fracture with no normalization, as compared to the mass. There are many ways in which the compressive force data could be normalized. Additional normalization schemes will be investigated once more sophisticated measuring tools are obtained, allowing for the direct measurement of hailstone volume.

Table 1: 2013 Mission #1 teams

Measurement Team 1	Measurement Team 2
Ian Giammanco – FC, Team Leader, DAQ Operator Hank Pogorzelski - Photographer Rose Grant (TRAIL)– Measurement	Tanya Brown – LC, Team Leader, DAQ Operator Doug Dewey (TRAIL) – Photographer Andy Stumpf – Measurement
Camera Probe Team 1	
Scott Fowler – Team Leader Brent Henzi – Team Member Heather Paul (SF)– Team Member	

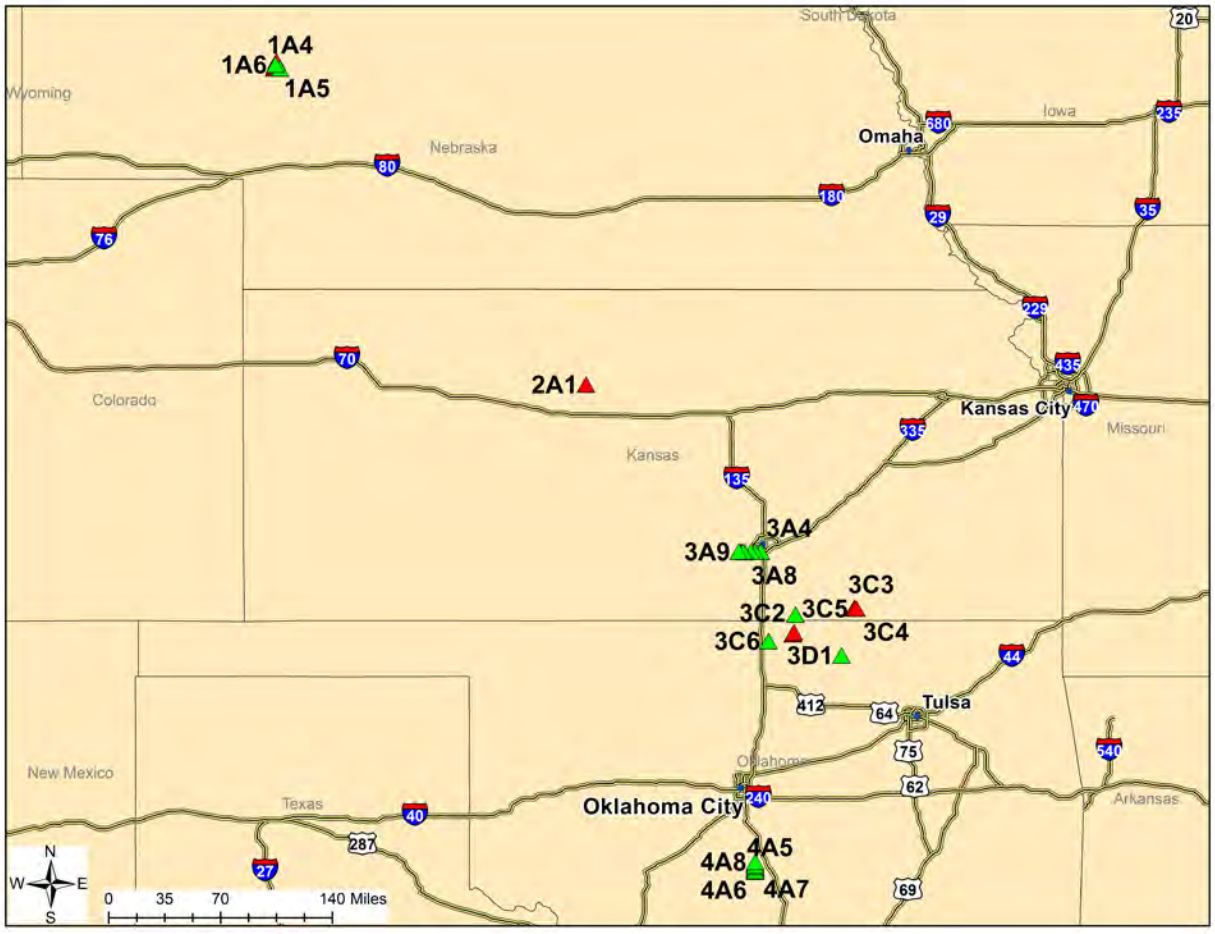


Figure 5: A map of Mission #1 deployment locations

Table 2: 2013 Mission #1 summary data

Deployment ID	Date	Location	Dual-Pol Coverage	No. stones measured	Largest stone dimension (inch)	Mean stone dimension (inch)	Smallest stone dimension (inch)	Maximum compressive stress (psi)	Mean compressive stress (psi)	Minimum compressive stress (psi)
1A1	05/17/2013	Hyannis, NE	KLNX	17	1.11	0.59	0.05	227	111	47
1A2	05/17/2013	Hyannis, NE	KLNX	17	0.72	0.44	0.04	673	206	8
1A3	05/17/2013	Hyannis, NE	KLNX	21	1.62	0.76	0.34	289	70	7
1A4	05/17/2013	Hyannis, NE	KLNX	13	0.98	0.52	0.31	131	95	56
1A5	05/17/2013	Hyannis, NE	KLNX	5	0.55	0.37	0.24	177	146	90
1A6	05/17/2013	Hyannis, NE	KLNX	12	1.30	0.61	0.28	200	87	21
2A1	05/18/2013	Paradise, KS	KEUX	6	0.72	0.38	0.11	41	41	41
3A1	05/19/2013	Wichita, KS	KICT	9	0.84	0.55	0.19	255	113	31
3A2	05/19/2013	Wichita, KS	KICT	15	1.03	0.68	0.35	213	84	20
3A3	05/19/2013	Wichita, KS	KICT	28	1.23	0.70	0.31	115	53	7
3A4	05/19/2013	Wichita, KS	KICT	8	0.94	0.52	0.20	624	298	98
3A5	05/19/2013	Wichita, KS	KICT	10	1.06	0.61	0.31	208	81	18
3A6	05/19/2013	Wichita, KS	KICT	15	0.98	0.52	0.20	485	78	1
3A7	05/19/2013	Wichita, KS	KICT	12	0.98	0.60	0.28	155	54	26
3A8	05/19/2013	Wichita, KS	KICT	10	1.26	0.66	0.28	112	58	19
3A9	05/19/2013	Wichita, KS	KICT	5	0.83	0.61	0.28	153	114	67
3B1	05/19/2013	Arkansas City, KS	KICT	6	1.35	0.72	0.31	101	35	11
3B2	05/19/2013	Arkansas City, KS	KICT	10	0.75	0.47	0.28	222	108	8
3C1	05/19/2013	Newkirk, OK	KICT/ KVNX	7	0.60	0.35	0.25	142	80	38
3C2	05/19/2013	Newkirk, OK	KICT/ KVNX	12	0.99	0.49	0.26	223	81	6
3C3	05/19/2013	Cedar Vale, KS	KICT	21	1.22	0.80	0.39	117	43	11
3C4	05/19/2013	Cedar Vale, KS	KICT	11	1.00	0.72	0.28	74	39	5

Table 2 continued: 2013 Mission #1 summary data

Deployment ID	Date	Location	Dual-Pol Coverage	No. stones measured	Largest stone dimension (inch)	Mean stone dimension (inch)	Smallest stone dimension (inch)	Maximum compressive stress (psi)	Mean compressive stress (psi)	Minimum compressive stress (psi)
3C5	05/19/2013	Cedar Vale, KS	KICT	39	1.57	0.94	0.39	165	46	5
3C6	05/19/2013	Blackwell, OK	KICT	4	0.55	0.43	0.28	101	81	56
3D1	05/19/2013	Burbank, OK	KINX	18	0.87	0.44	0.20	265	141	43
4A1	05/20/2013	Antioch, OK	KTLX	34	1.82	1.04	0.49	132	52	5
4A2	05/20/2013	Antioch, OK	KTLX	32	1.89	1.05	0.43	105	48	4
4A3	05/20/2013	Maysville, OK	KTLX	29	1.46	0.87	0.43	491	68	8
4A4	05/20/2013	Antioch, OK	KTLX	28	1.57	0.80	0.16	189	99	13
4A5	05/20/2013	Antioch, OK	KTLX	24	1.65	0.90	0.39	153	94	33
4A6	05/20/2013	Maysville, OK	KTLX	27	1.38	0.71	0.16	240	116	59
4A7	05/20/2013	Maysville, OK	KTLX	29	1.06	0.63	0.31	204	96	33
4A8	05/20/2013	Maysville, OK	KTLX	9	1.10	0.49	0.24	202	91	24

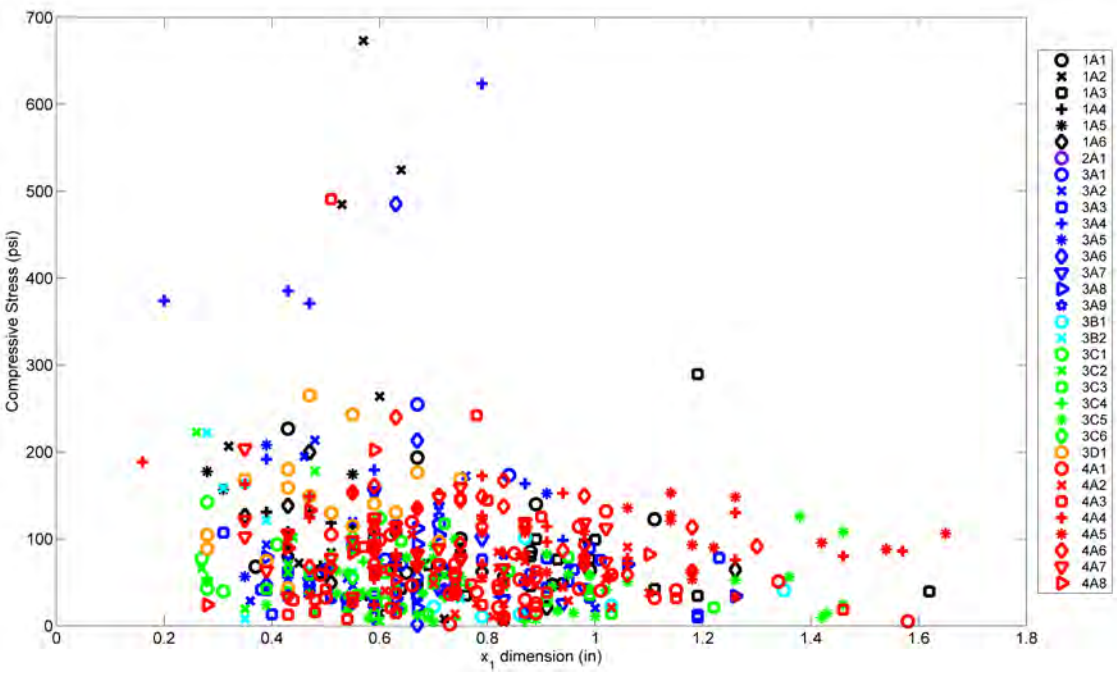


Figure 6: Compressive stress shown as a function of the x_1 dimension. Each colored circle represents observations from a single parent thunderstorm, while additional symbols of the same color represent more than one deployment on a parent thunderstorm.

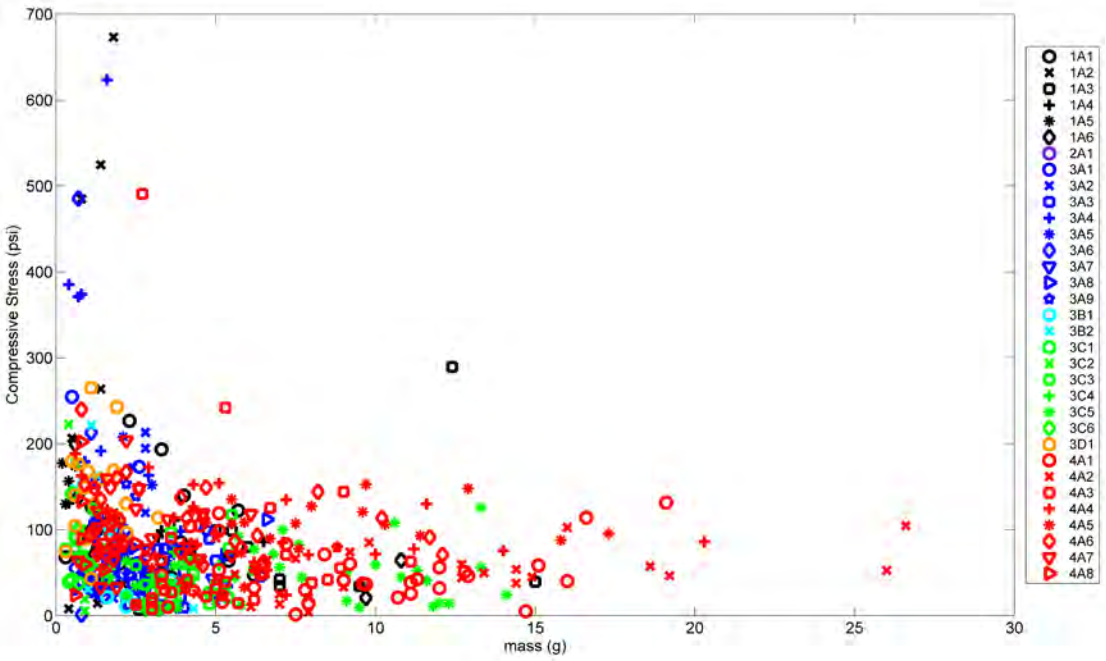


Figure 7: Same as Figure 6 except compressive stress is shown as a function of mass.

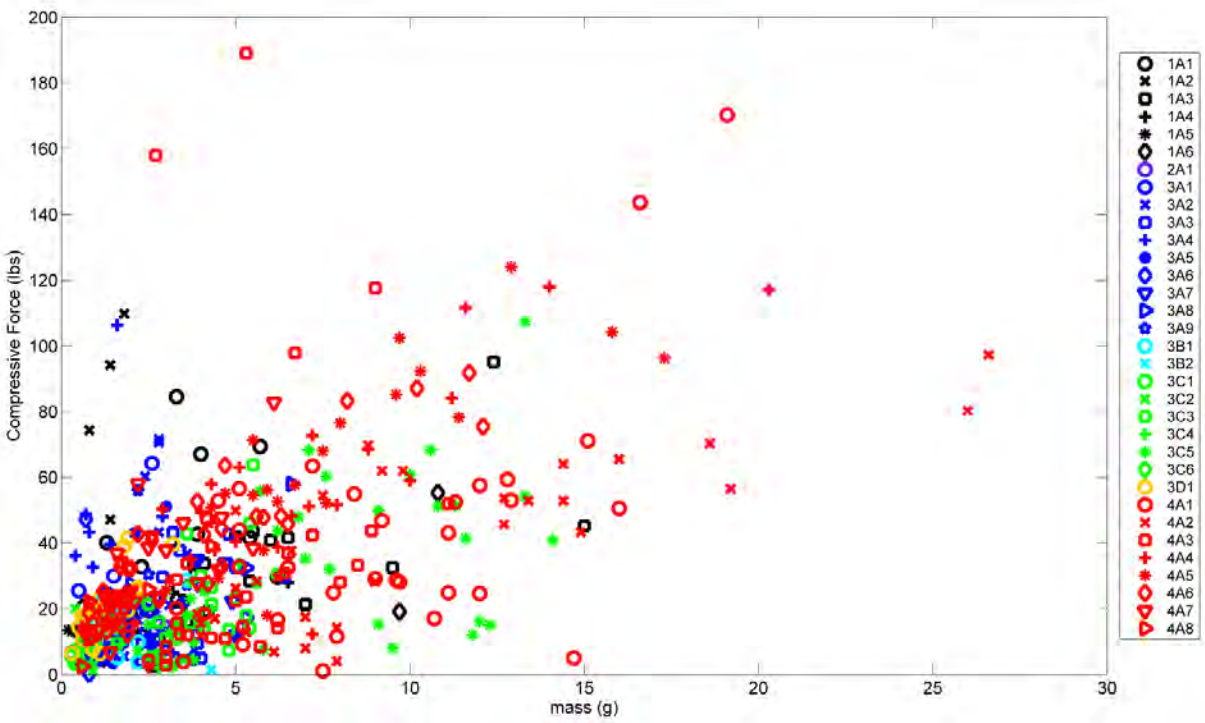


Figure 8: Compressive force at fracture (non-scaled) shown as a function of mass. Symbols and colors are the same as Figure 6 and 7.

Although there is some evidence of clustering of data by parent thunderstorm shown in Figure 6 through Figure 8, the compressive stress dependence is not as apparent as it was in the 2012 dataset. There are more data points in the 2013 dataset, and there is more scatter amongst the data. It is important to note again that the largest stone is not the hardest stone. From these data, the stones with the highest compressive stresses generally came from storm 1A near Hyannis, Nebraska on May 17 and from storm 3A in Wichita, Kansas on May 19. Storm 3A will be discussed in more detail in the next section. Additional work exploring the environmental characteristics which led to the higher compressive stress values of measured hailstones in these two storms will be conducted in the future.

5.1.1 Case Studies

One of the primary goals of the 2013 field study was to attempt to make higher spatial resolution measurements from a given parent thunderstorm such that the swath of hailfall was well-documented. It was important to use two deployment teams to achieve this goal. Through a "leap-frog" strategy, on several occasions the two teams were able to quickly collect data across the region of hailfall at spatial resolutions of 1 to 2 miles on a single road. This section presents two individual cases from two separate parent thunderstorms during Mission #1 in which a high spatial resolution dataset was collected across the hail swath. Observations also were compared to radar-derived maximum expected hail size swaths from the National Severe Storms Laboratory (NSSL) near-real time Warning Decision Support System of Integrated Information (WDSSII; Lakshamanan et al., 2007). This system leverages multiple radars to

produce a swath of maximum expected size of hail (MESH) for a 1 km by 1 km grid resolution over a specified spatial and temporal domain (Witt et al., 1998; Stumpf et al., 2004).

5.1.1.1 Case Study 1: May 19 in Wichita, Kansas

The first case study covers operations on May 19, 2013 as the deployment teams targeted a high-precipitation, tornadic, supercell thunderstorm within the western portion of the Wichita, KS metropolitan area. The target storm rapidly developed along an outflow/stationary frontal boundary and propagated east-northeastward toward Wichita, eventually moving through the city. The supercell became tornadic as it approached the selected deployment roadway. The radar reflectivity image shown in Figure 9 shows the target thunderstorm shortly before it crossed the data collection roadway. Because of the storm's tornadic nature, sufficient lead time was not available to ensure a safe Camera Probe deployment.

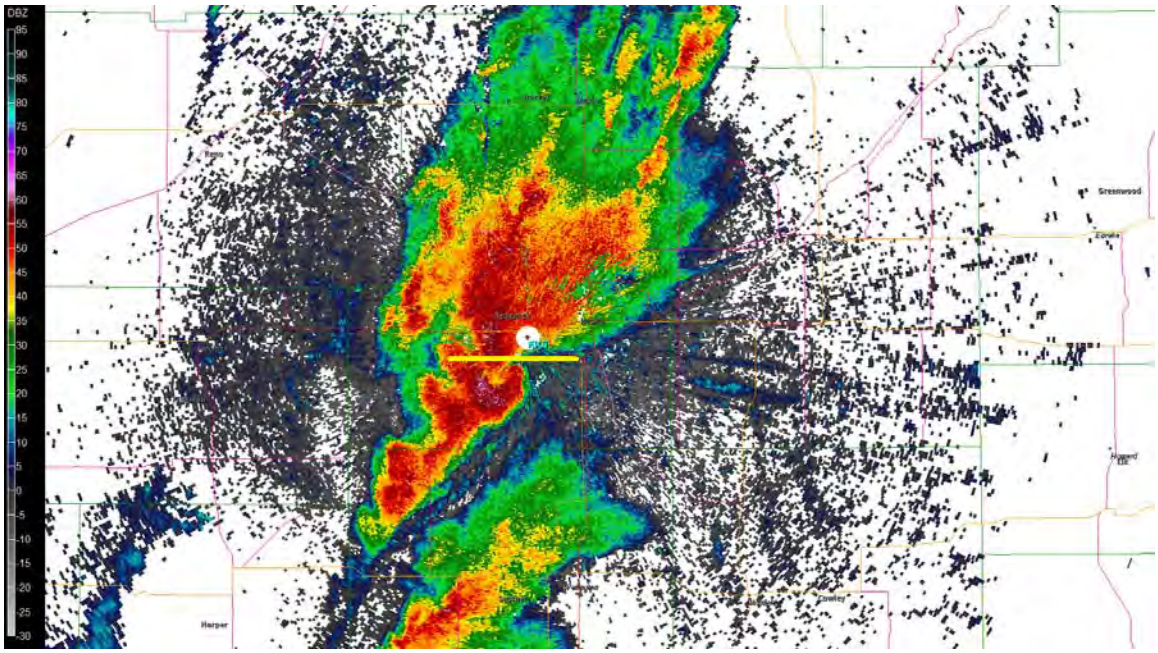


Figure 9: Radar 0.5 degree reflectivity from the KICT WSR-88D radar at 2036 UTC on May 19, 2013. The solid yellow line represents the approximate measurement swath.

Data collection began approximately 10 minutes after the storm had passed the roadway when it was safe to proceed. Measurement stops were made at approximately 1 to 1.5 mile intervals using a "leap-frog" strategy as both teams remained on the same road. The maximum measured sizes were between 0.9 and 1.26 inches and were primarily found within the western portion of the data collection swath. This region was located in a storm-relative location immediately left (north) of the mesocyclone/tornadic circulation, which is a favored region for large hail (Browning 1964; Lemon and Doswell, 1979). Data collection deployments were made along an east-west roadway which was not perpendicular to the long axis of the swath as a result of the general storm motion. In general, the mean and peak compressive stress values across the deployment swath were similar except at the initial

measurement location (Deployments 4A1-team 1 and 4A4-team 2). This location contained several relatively hard but sub-severe stones (diameter < 1 in.). This region was within the rear-flank downdraft such that stones may have quickly been forced downward from within the parent thunderstorm. Given such hard stones, detectable damage as a result of wind-driven hail within this narrow region may have been plausible even with smaller stones. It is noted that in general the stones with the largest compressive stress did not necessarily correspond to the largest mean or maximum sizes which is in good agreement with the results from the 2012 pilot field study (Brown et al., 2012; Giammanco and Brown, 2013).

This specific case resulted in nine individual data collection locations, in which a total of 112 stones were measured across the swath of hail. Figure 10 provides a spatial comparison of observations with the radar-derived MESH swath. For this case, the Wichita (KICT) WSR-88D radar was located only a few miles from the deployment roadway such that the radar beam height was only 300-400 ft. above the deployment roadway. Although the WDSSII MESH algorithm assimilates data from multiple radars, the close proximity of the KICT radar should provide optimum estimates of maximum hail size relative to ground deposition. When the supercell crossed the deployment roadway it produced hail sizes up to 1.26 in. with mean compressive stress values across the swath slightly larger than the mean from the complete 2012-2013 dataset. As shown in Figure 10, the MESH algorithm slightly overestimated the maximum hail size by a mean of 0.24 in. compared to those stones measured by the deployment teams. It is encouraging that radar-derived estimates matched the observations reasonably well, and effectively captured the shape of the two local maxima within the swath (Figure 10). It is noted that the measured hail size distribution at each location is representative of mean sizes greater than 0.5 in. The MESH algorithm and dual-polarization hydrometeor classification algorithm from the KICT radar both suggested that hail deposition occurred at locations west of deployment 3A9, but the measurement teams were unable to locate any. This may be a result of un-measurable small stones and/or melting of small stones prior to the measurement teams arriving to collect and measure them. Significant precipitation would likely have caused the complete melting of small stones prior to measurement. It could also be due to errors in radar estimates of hail occurrence and maximum size which are known to exist within the conventional WSR-88D derived products (Edwards and Thompson, 1998).

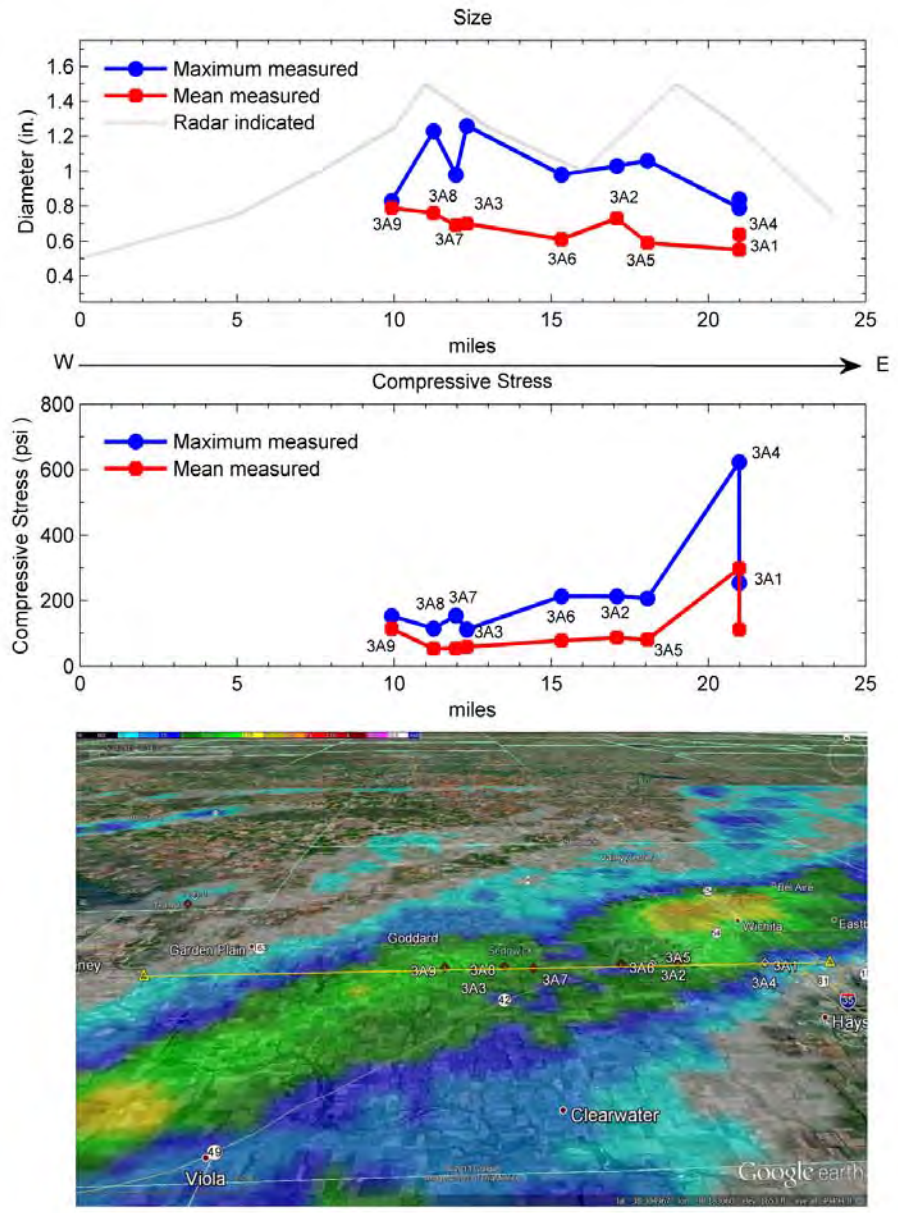


Figure 10: Measured peak (blue), mean (red) hail size (top) and compressive force (middle) at each deployment location compared with the WDSSII MESH hail swath (bottom). The yellow line indicates the spatial domain of field measurements.

5.1.1.2 Case Study 2: May 20 in Antioch/Maysville, Oklahoma

The second case study occurred on May 20, 2013 near Antioch, OK. The measurement teams targeted a non-tornadic supercell thunderstorm approximately 40 miles south of the Oklahoma City metropolitan area, shown in Figure 11. While the deployment teams were positioning, a separate supercell developed near Newcastle, OK and produced the violent EF-5 tornado which passed through Newcastle and Moore.

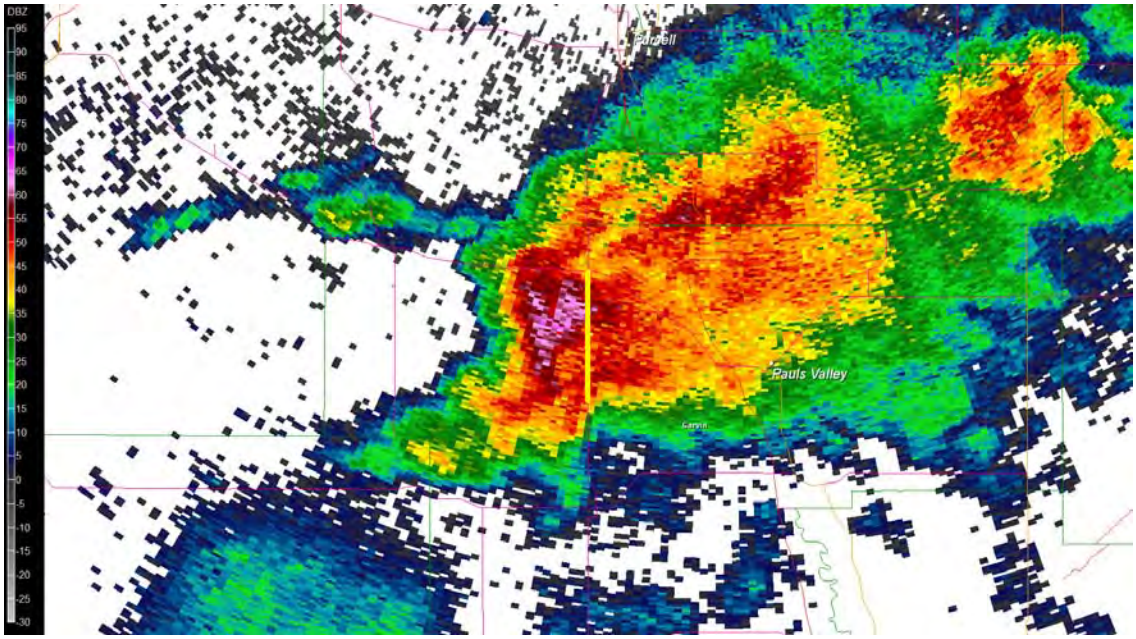


Figure 11: Radar 0.5 degree reflectivity from the KTLX WSR-88D at 2133 UTC on May 20, 2013. The solid yellow line corresponds to the approximate measurement swath.

The target supercell evolved from a broken line of three separate rotating thunderstorm updrafts which developed along a dryline, southwest of Oklahoma City. These cells eventually merged, resulting in a discrete high-precipitation supercell which propagated nearly due east. The deployment teams initially positioned to the east of the cluster of cells. As the merger took place and it became apparent that a more discrete supercell structure was taking shape, Measurement Team 1 and the Camera Probe Team positioned for a probe deployment near Antioch, OK. The deployment targeted the region to the immediate north (storm-relative left) of the mesocyclone and updraft where large hail would be expected.

The deployment featured eight measurement locations along a single north-south oriented roadway with co-located measurements at the Camera Probe deployment site. The measurement domain was nearly perpendicular to the radar-indicated swath of hailfall, providing a quality sample of the characteristics of hail directly across the axis of the swath. Figure 12 provides a spatial analysis of the characteristics of hail across the swath and a comparison with the WDSII MESH algorithm. For this case, the KLTX WSR-88D radar was located approximately 40 miles to the north-northeast which resulted in a radar beam height for the 0.5° tilt angle of 2700 ft. Similar to the first case, the maximum hail size across the swath exhibited a double maxima shape. The maximum measured size across a 2 to 3 mile stretch was between 1.5 in. and 2 in., with all but two measurement locations exceeding the radar-estimated maximum hail size. The MESH algorithm provided a mean underestimate of 0.31 in. in maximum hail size across the measurement domain. As seen in the 2012 study and the previous case, the peak compressive stress values within the domain were not correlated with the largest measured stones.

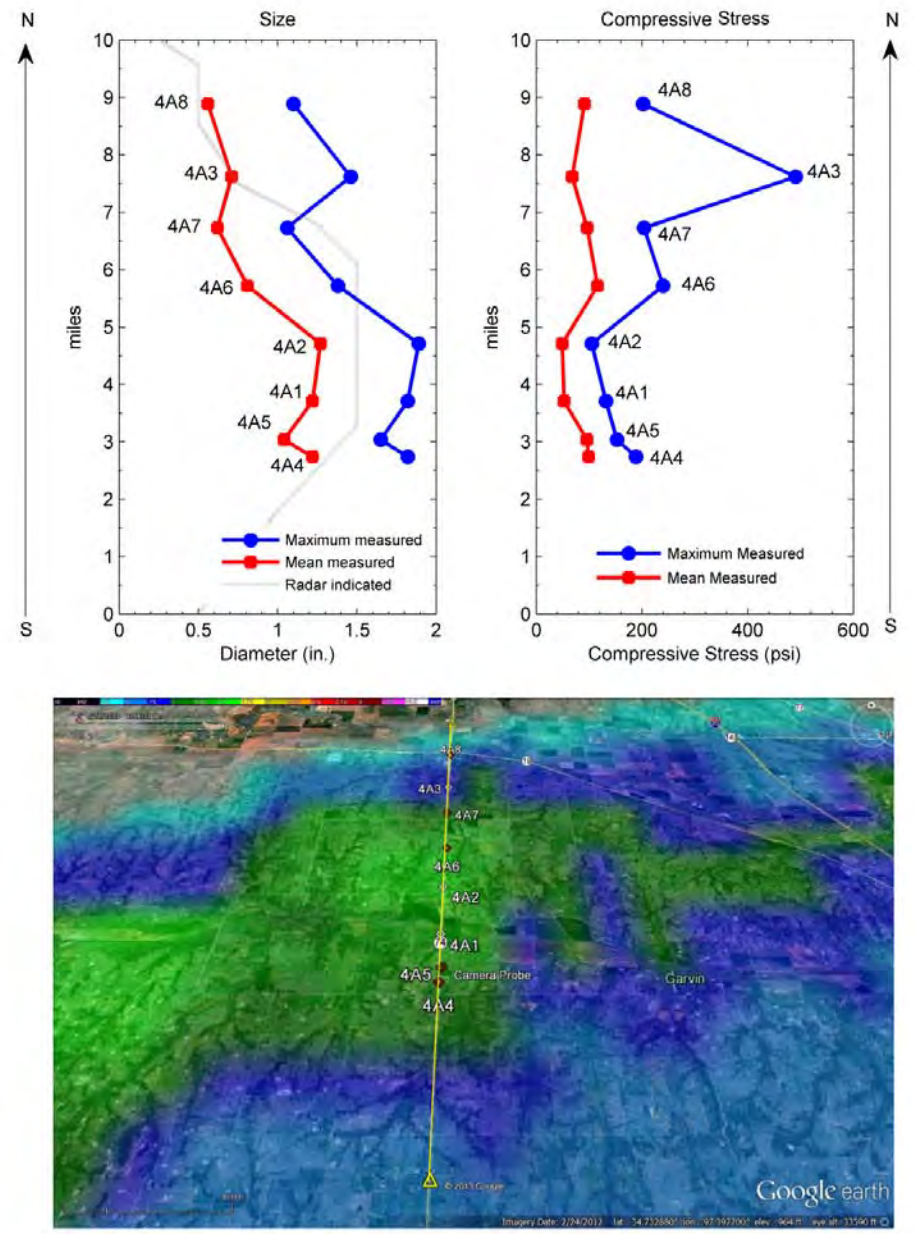


Figure 12: Measured peak (blue), mean (red) hail size (top-left), and compressive stress (top-right) at each deployment location compared with the WDSSII MESH hail swath (bottom). The yellow line indicates the spatial domain of field measurements shown in the data comparison.

Subjective analysis of the camera probe imagery revealed a more complex storm structure and an interesting evolution of the precipitation pattern. As discussed previously, the target storm was the result of a merger of three cells; however imagery revealed that the northern cell in the cluster retained its mesocyclone circulation which was easily captured by the camera probe as it passed north of Antioch, OK. A video capture from camera #3 within the probe at 2109 UTC is shown in Figure 13 along with the associated radar image. This feature eventually weakened and a more discrete supercell

developed further southwest. This discrete cell and its associated hail core passed over the probe later in time, as shown in the timeline in Figure 14. The timeline was created from imagery analysis which revealed several short duration windows of heavy rain and small hail that was not effectively captured by the KTLX radar dual-polarization hydrometeor classification algorithm which indicated strictly rainfall until 2129 UTC with heavy rain and hail indicated through 2133 UTC. Camera probe imagery suggested a hailfall temporal window from 2129 through 2139 UTC with variability in size and frequency within that domain as shown in Figure 14. There was a 1-minute period in which hail appeared to cease. The error in the radar-derived window of hail may be a result of the coarse temporal sampling strategies of WSR-88D radars as well as the relatively high minimum beam height. Significant radar reflectivity (> 60 dBZ) was observed from 15,000 to 30,000 ft as the target storm crossed the deployment roadway. Such values at high altitudes are a signature of hail which may have fallen during the time period required for the radar to complete its subsequent volumetric sampling pattern. The differential reflectivity (Z_{DR}) vertical cross-sections derived from dual-polarization data at this time also support this assessment with values near zero which are typically associated with hail (Van Den Broeke et al., 2008; Kumjian and Ryzhkov, 2008).

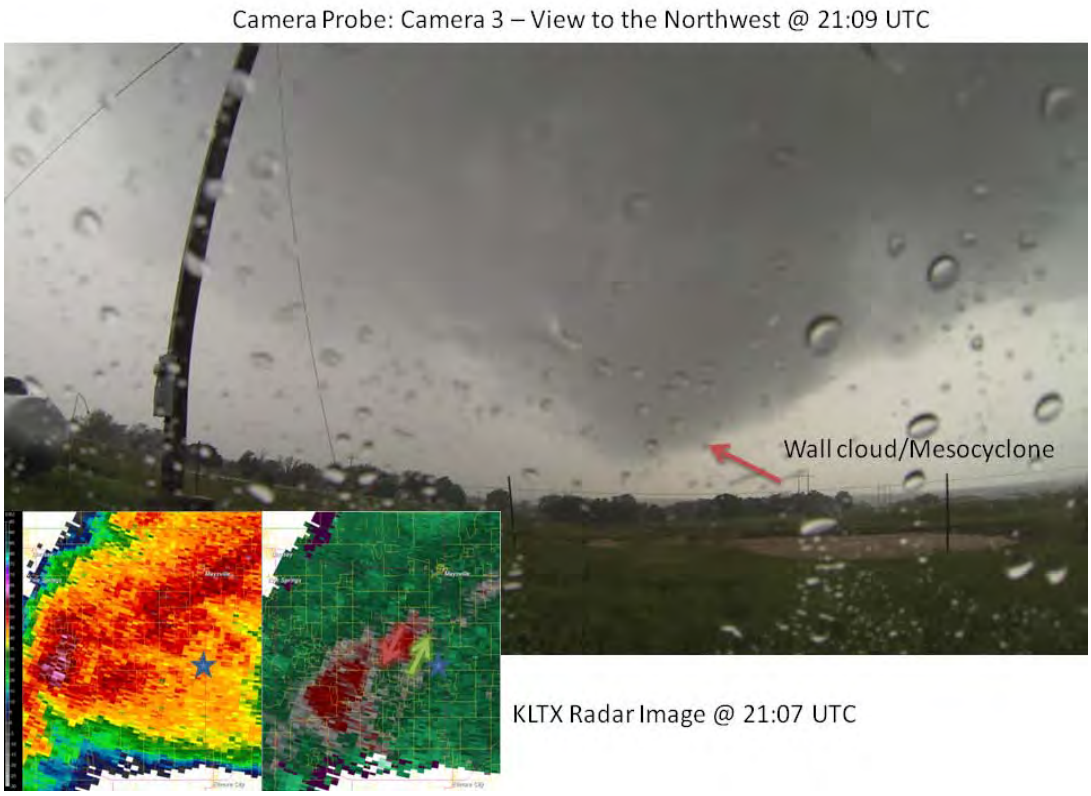


Figure 13: Image from camera #3 at 2109 UTC and associated KTLX radar reflectivity at 2107 on May 20, 2013. The blue star denotes the location of the probe.

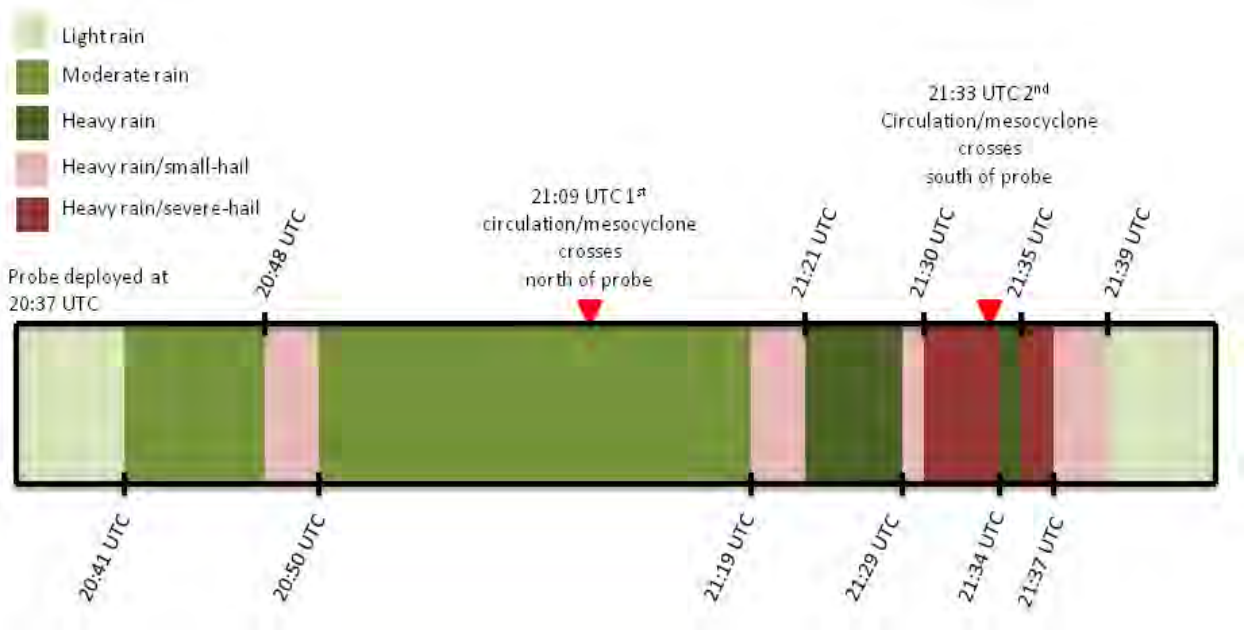


Figure 14: Estimated timeline of the evolution of the precipitation pattern derived from subjective analysis of imagery collected by the Camera Probe from 2037 UTC through 2145 UTC on May 20, 2013.

The maximum visually-estimated size and frequency of hail at the Camera Probe location occurred at 2136 UTC with two to three impacts per second on the Lexan dome of the Camera Probe (surface area of 2.25 ft^2). The maximum measured hail size at the probe location was 1.65 inches. Based on the collected imagery, stones of 1 inch or greater likely occurred in a relatively short time period from 2130-2132 UTC and then from 2135-2136 UTC. Imagery also indicated relatively vertical trajectories with no evidence of strong winds. This was expected given the storm-relative location of the probe to the left of the direction of motion of the second mesocyclone. Typically within a supercell thunderstorm, the strongest winds are found within the rear-flank downdraft (storm-relative right of the mesocyclone direction of motion) which would be the area to anticipate wind driven hail (Dowell and Bluestein, 1997; Markowski et al. 2002; Lee et al., 2004; Shabbott and Markowski, 2006; Hirth et al., 2008; Skinner et al., 2011; Lee et al., 2012). This region is not the favored location for the largest hail sizes (Browning, 1964; Lemon and Doswell, 1979; Doswell and Burgess, 1993; Moller et al., 1994).

From the radar data, the storm motion was estimated to be nearly due east at 25 mph. A simple time-to-space conversion based upon the timeline derived from the Camera Probe imagery was used to yield a longitudinal (east-to-west) spatial domain of hailfall of approximately 4 miles with a lateral (south-to-north) dimension of approximately 6.5 miles as determined by the measurement teams. The crude estimate assumes the parent thunderstorm is in a steady state. The basic analysis presented here highlights the value of any deployable system that can provide information on the variability of hail within a thunderstorm. The development of a network of rapidly-deployable impact devices that can provide a time history of hail sizes could lead to a highly accurate assessment of both the spatial and temporal distribution of hail within a parent thunderstorm. These data can be used to produce accurate

large test chamber simulations of specific cases, yielding a more complete picture of a given hail event for risk modeling applications.

5.2 Mission #2

The second mission of 2013 took place from May 30 to June 5. Mission #2 team members are listed in Table 3 and included only IBHS personnel. The teams arrived in Oklahoma City, Oklahoma and traveled to New Mexico, Oklahoma, and Texas and successfully collected six datasets on hailstones from four parent thunderstorms on three operations days as shown in Figure 15. Table 4 provides summary statistics from Mission #2. The majority of hailstones measured were still less than 1 in. in diameter, but at each deployment site the team measured at least one stone larger than 1 in., including a 4.21 in. hailstone from storm 5B, which is the largest stone measured in the two-year history of the project. The compressive forces were normalized as described previously and are shown in Figure 16 as a function of the x_1 dimension and in Figure 17 as a function of mass. The data with no normalization scheme is presented as a function of mass in Figure 18.

Table 3: 2013 Mission #2 teams

Measurement Team	Camera Probe Team
Ian Giammanco – FC, Team Leader, DAQ Operator	Scott Fowler – Team Leader
Hank Pogorzelski - Photographer	Brent Henzi – Team Member
Eddie Cranford – Measurement	

There is greater evidence of data clustering by parent thunderstorm within the Mission #2 data. Hailstones measured from storm 6A showed a large range in variability of compressive stress, while the range of sizes measured was quite small. Hailstones measured from storms 5B and 7A showed a larger variability in the range of sizes measured, with relatively smaller variability in the measured compressive stresses. It is important to note again that the largest stone is not the hardest stone.

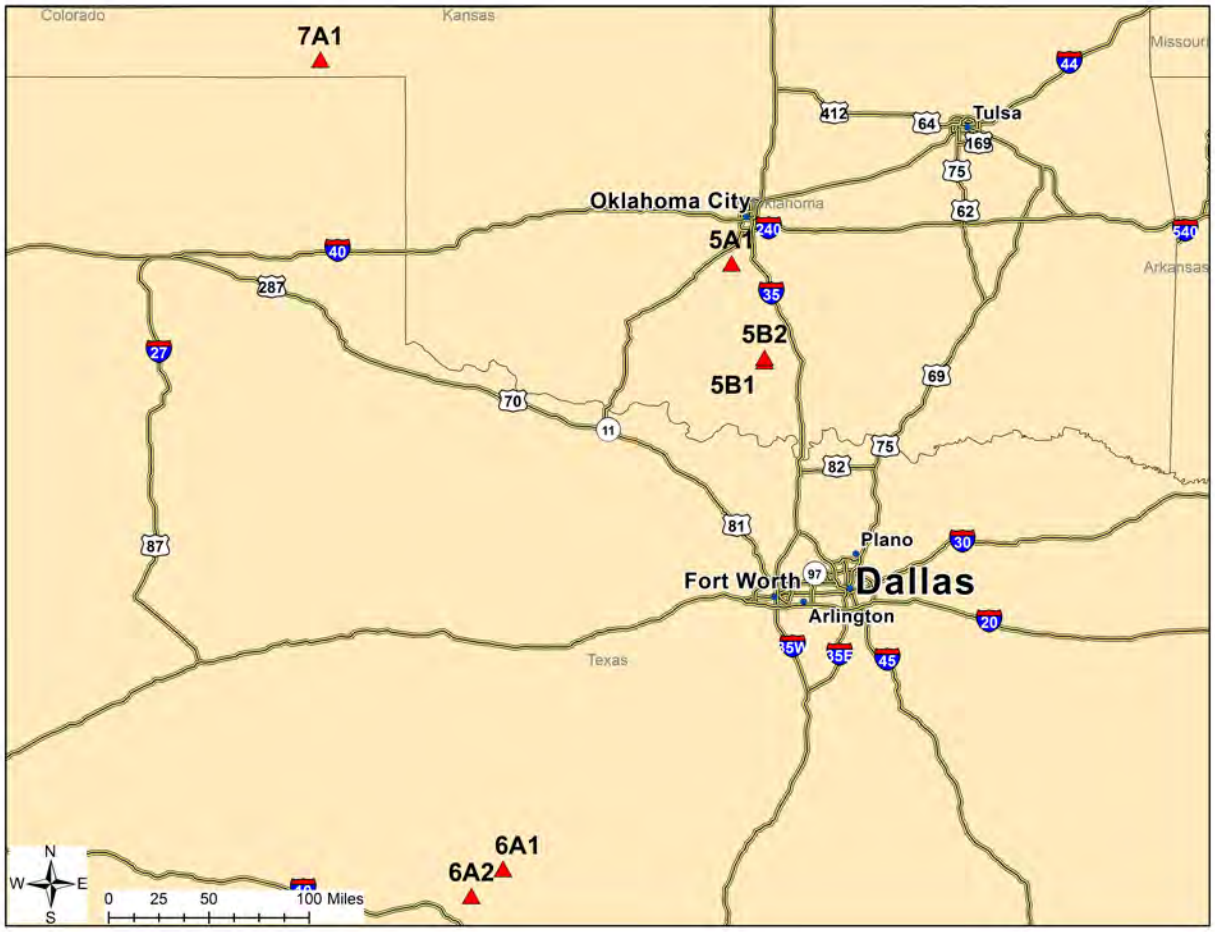


Figure 15: Map of Mission #2 deployments.

Table 4: 2013 Mission #2 summary data

Deployment ID	Date	Location	Dual-Pol Coverage	No. stones measured	Largest stone dimension (inch)	Mean stone dimension (inch)	Smallest stone dimension (inch)	Maximum compressive stress (psi)	Mean compressive stress (psi)	Minimum compressive stress (psi)
5A1	05/30/2013	Blanchard, OK	KTLX	15	1.57	0.82	0.37	233	88	12
5B1	05/30/2013	Ratliff City, OK	KTLX	10	1.83	0.86	0.41	571	127	9
5B2	05/30/2013	Ratliff City, OK	KTLX	19	4.21	1.20	0.47	182	79	21
6A1	06/01/2013	Mason, TX	KSJT	29	1.18	0.63	0.28	1097	242	51
6A2	06/01/2013	London, TX	KSJT	30	1.42	0.74	0.28	951	211	29
7A1	06/02/2013	Elmwood, OK	KDDC	36	1.46	0.74	0.43	420	75	8

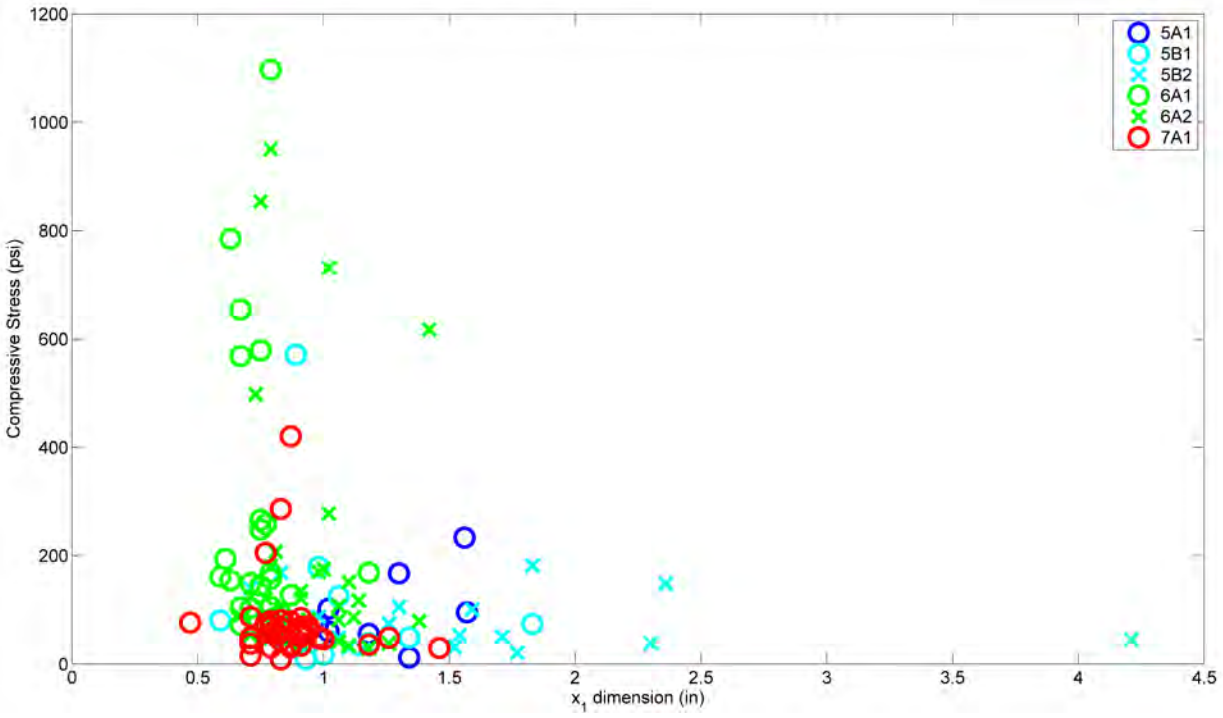


Figure 16: Compressive stress shown as a function of the measured x_1 dimension. Each colored circle represents observations from a single parent thunderstorm, while additional symbols of the same color represent more than one deployment on a parent thunderstorm.

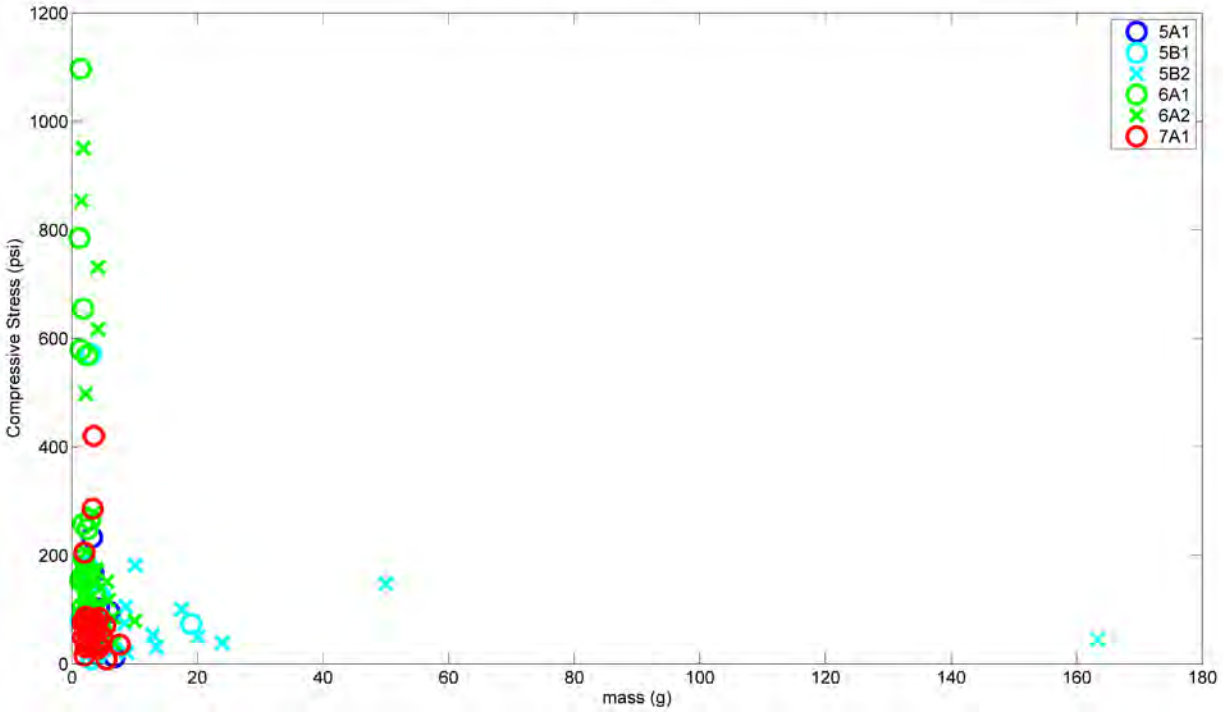


Figure 17: Same as Figure 16 expect shown as a function of mass.

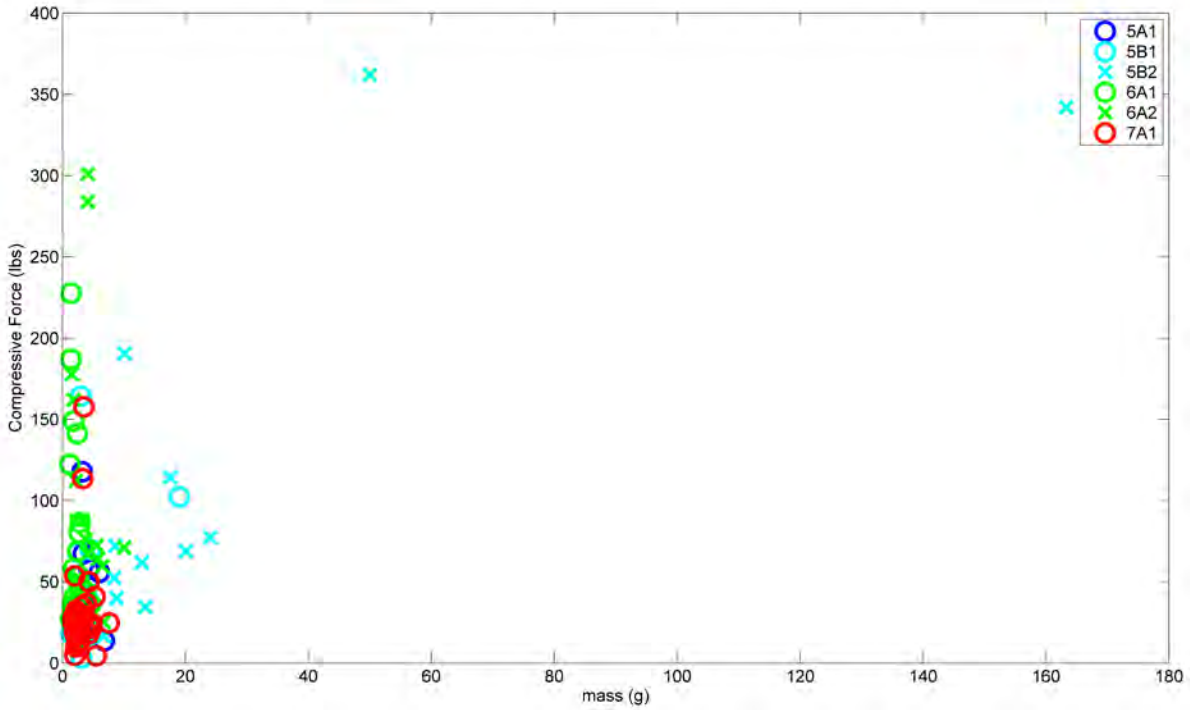


Figure 18: Compressive force at fracture (non-scaled) shown as a function of the measured mass. Symbols and colors the same as Figures 16 and 17.

6 Application of Field Observations in Laboratory Testing

6.1 Mass and Diameter

The relationship between mass and hailstone diameter is understood relatively well and follows an exponential relationship (Dennis et al. 1971; Brown et al., 2012). It is also expected that the kinetic energy associated with a given stone will influence its ability to produce damage. The kinetic energy is dependent on the mass and fall speed which is dependent on the aerodynamic drag of the stone. The aerodynamic drag in turn is dependent on the shape and size of the stone. For non-spherical stones, kinetic energy is also influenced by the orientation of the stone as it falls, as well as its orientation with regards to the wind field through which it is falling and whether the stone is tumbling. Theoretically, each individual stone has a different drag coefficient dependent upon these characteristics. Historical literature suggests that the drag coefficient of natural hailstones varies from 0.45 to 0.9 (Laurie, 1960; Macklin and Ludlum, 1961; Lozowski and Strong, 1978; Beattie, 1979; Matson, 1980). Small oblate hailstones were found to fall nearly 50% slower than a sphere of the same diameter (Roos and Carte, 1973). It is generally accepted that natural hail typically does not reach the theoretical terminal velocity for a spherical shape of the same diameter (Knight and Heymsfield, 1983; Khorostynov and Curry, 2005; Heymsfield and Westbrook, 2010).

The mass/diameter relationship was examined for laboratory hailstones and those collected during the 2012 and 2013 field studies. The results are shown in Figure 19. The laboratory stones do fall within the range of those observed in the field but represent the upper-bound of natural hail. For all liquid solutions used in laboratory experimentation, stones were typically biased towards a higher mass given a similar diameter, as compared to the field hailstones. The primary cause is the use of purely spherical laboratory stones while typical hailstones are not perfect spheres with a large portion of the dataset resulting from disc-shaped spheroids which have a smaller volume and mass as described by Figure 20. This suggests that for a given diameter, spherical laboratory stones would generally possess a larger kinetic energy upon impact than a natural hailstone of equal diameter, because of the larger mass associated with the spherical shape as compared to disc or other shapes. Current impact testing standards likely are representative of the upper bound of impact energy imparted on a surface by the specified sizes of hailstones given no wind effects. Differences also likely arise from the freezing process used in the laboratory versus the natural hail growth processes as well as the porosity of natural hail.

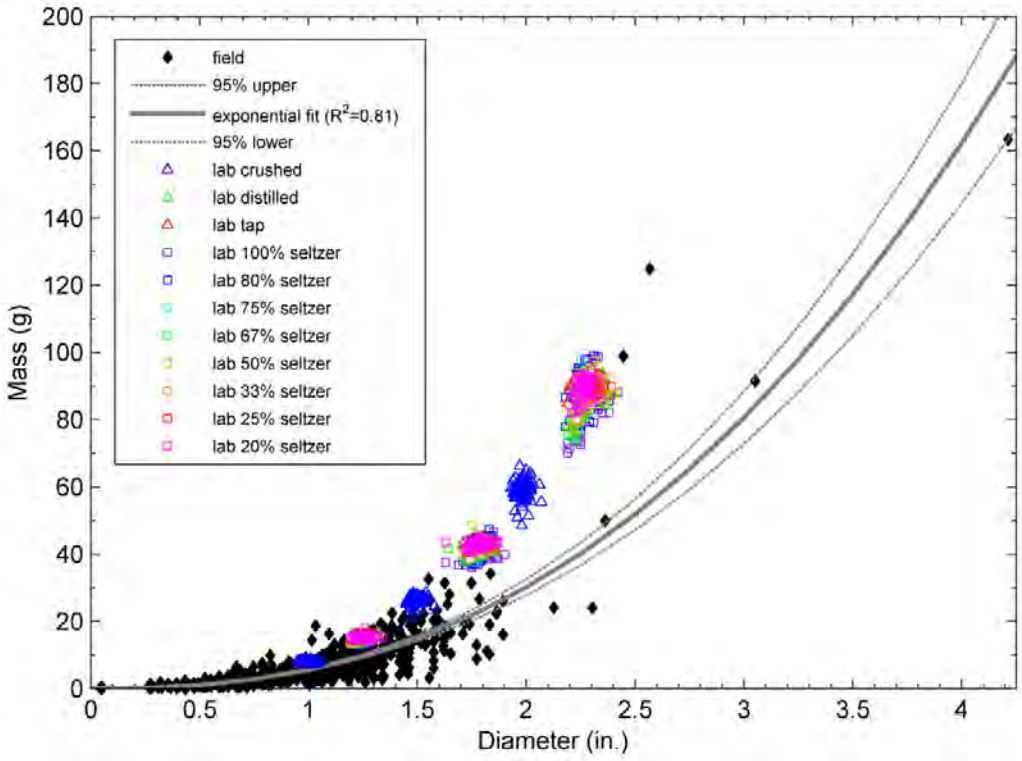
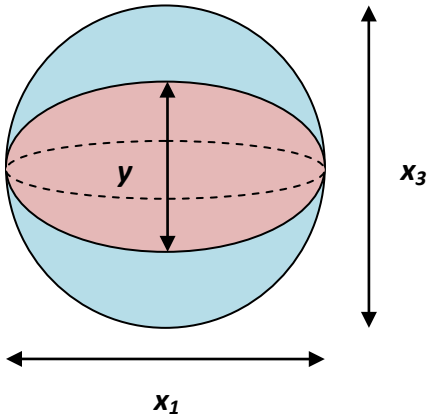


Figure 19: Comparison of mass-diameter relationship for field and laboratory hailstones. A best-fit exponential relationship is shown (solid) along with the 95% confidence intervals (dashed).



$x_3 > y$
VOLUME OF SPHERE > VOLUME OF DISC SPHEROID
MASS OF SPHERE > MASS OF DISC SPHEROID

Figure 20: Schematic of differences in dimensions and associated volumes for spheres vs. disc-shaped spheroids.

6.2 Kinetic Energy

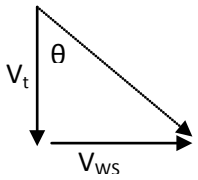
The theoretical impact kinetic energy of hailstones cataloged during the 2012 and 2013 field studies was examined along with the contribution of a uniform horizontal wind. Theoretical values also were compared with assumptions included in hail impact test standards (e.g. UL 2218, FM 4473) to understand expected product performance when subjected to more natural hail impacts. To estimate the energy at impact of a given stone, the fall velocity at impact is needed. The terminal velocity of a given stone represents the upper bound of possible fall speeds in the absence of wind. The theoretical terminal velocity is expressed as:

$$V_t = \left(\frac{2mg}{\rho_{air} A C_D}\right)^{\frac{1}{2}} \quad (1)$$

where m is the mass of the object, g is gravity, ρ_{air} is the density of air (at the surface ~ 1.23x10^{-3} g cm^{-3}), A is the surface area of the stone, and C_D is the aerodynamic drag coefficient. For a spherical shape, Equation 1 becomes:

$$V_t = \left(\frac{4\rho_{hail} g}{3\rho_{air}\ C_D}\right)^{\frac{1}{2}} D^{\frac{1}{2}} \quad (2)$$

where ρ_{hail} is the density of natural hail (for this comparison it is assumed to be 0.6 g cm^{-3} from Browning et al., 1963, and D is the diameter of the stone (for measured hailstones this is the larger of the x_1 and y_1 dimensions). It is noted that density calculations using the measured x_1 and y_1 dimensions and associated mass are subject to large errors as a result of assuming a spheroidal shape. These errors result from the non-homogeneous surface of natural hail which are not perfect spheroids. The drag coefficient for this investigation was assumed to be a constant 0.61 for each stone (Beattie, 1979). This value is near the median for the range of drag coefficients discussed in historical literature and representative of rough spheres (Matson and Huggins, 1980). To account for the basic effects of a uniform horizontal wind profile, the fall speed was calculated by:

$V_{final} = \left({V_t}^2 + {V_{WS}}^2\right)^{\frac{1}{2}}$ for: 

(3)

where V_{WS} is the horizontal wind vector and θ is the angle of impact on a horizontal surface. It is noted that a falling object (e.g. hail) will lag the true wind field in its motion (Lally and Leviton, 1958). It is also noted that observed thunderstorm vertical wind profiles are far more complex (Gunter and Schroeder, 2013) and a more detailed modeling effort is needed to understand variability in hail impact angles. The calculated impact velocity was used to estimate the total kinetic energy of the stone at impact through:

$$KE = \frac{1}{2} m {V_{final}}^2 \quad (4)$$

where m is the mass of the observed hailstones and V_{final} is the velocity at impact.

The theoretical kinetic energies for two wind speed cases (10 mph and 60mph constant winds) are presented in Figures 21 and 22. The comparison is idealized but provides valuable information regarding the expected performance of rated materials when impacted with natural hailstones instead of the standard test method projectiles. The dataset collected by IBHS in 2012 and 2013 cannot be assumed to represent the hail size distribution from any given hail-producing thunderstorm. However, this comparison represents the upper bound of the impact energies that would be obtained for the observed size distribution. As shown in Figure 21, the Class 4 rating for both test standards encompasses a large percentage of observed hailstones (99%) at low horizontal wind speeds. By increasing the horizontal wind speed to 60 mph (National Weather Service severe wind criteria is 55.7 mph), the overall distribution shifts toward higher kinetic energies for a given diameter and impact angles approach 45° for stones less than 1.5 inches in diameter, where 90^{o} is a vertical impact. It is noted that observed natural hail mean impact angles in the presence of wind typically range from 58 to 75° with only the most extreme cases reaching 45° (Changnon, 1973).

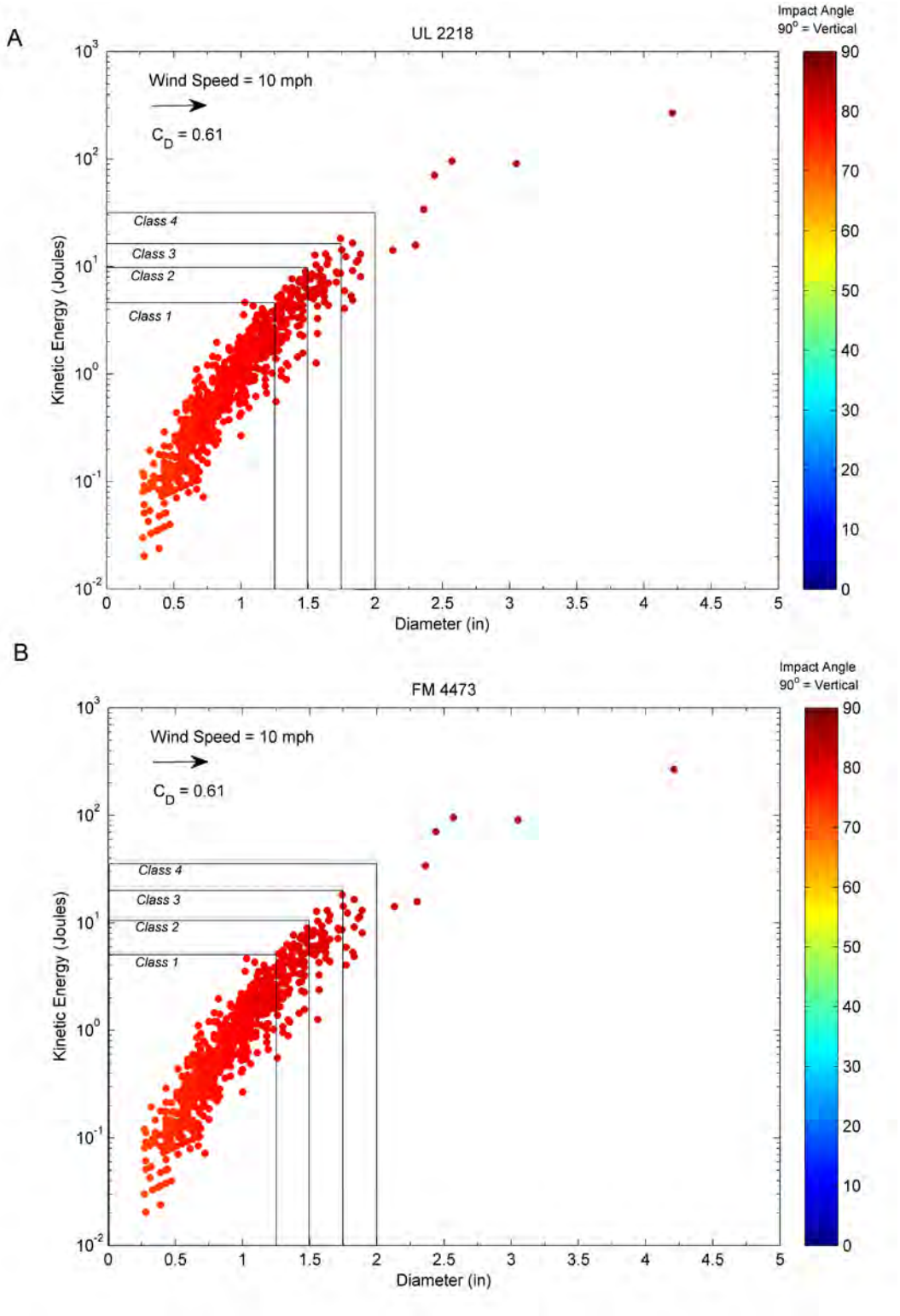


Figure 21: Estimated impact kinetic energy for a horizontal wind speed of 10 mph shown as a function of diameter for measured natural hailstones (2012 and 2013), compared to (A) UL 2218 (2012) steel ball material performance ratings and (B) FM 4473 (2005) ice ball material performance ratings. Hailstones are contoured by calculated angle of impact (90° represents a true vertical trajectory).

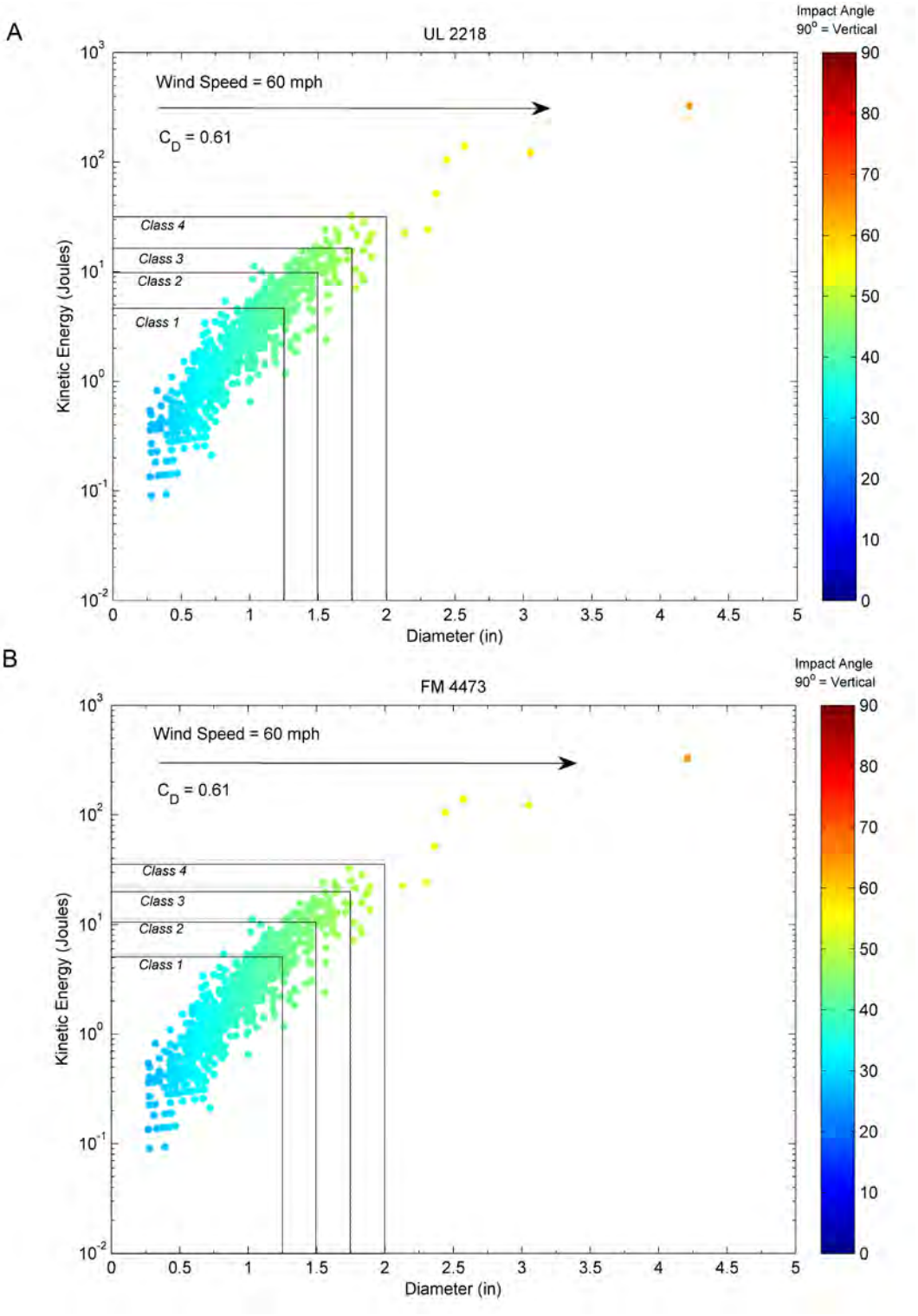


Figure 22: Same as Figure 21 but for a uniform horizontal wind of 60 mph.

It is interesting to note in the low wind speed case in Figure 21, the theoretical kinetic energies of nearly all measured hailstones fall within the kinetic energy range for that impact test class of projectile; i.e. there are no 1.25 in. measured hailstones whose theoretical kinetic energy exceeds that of the Class 1 threshold, for either the UL 2218 or FM 4473 test standards. However, with the increase in theoretical kinetic energy associated with an assumed constant horizontal wind of 60 mph, there are a large number of measured hailstones whose theoretical kinetic energies exceed their impact test class designations; i.e. there are a large number of measured hailstones of approximately 1 in. to 1.25 in. that fit the size range of a Class 1 projectile, but have theoretical kinetic energies approaching those of a Class 2 projectile. It is noted that the surface-relative angle of impact (e.g. roof slope, walls) will influence the duration of impact and the surface area in which energy is transferred to the material.

It is expected that the degree of damage to a given material will scale primarily with the energy passed to the material at impact and the surface area in which that energy is absorbed. Accurately quantifying the true impact energetics of natural hailstones is dependent upon quality measurements of the dimensions and masses as well as the ability to correctly assess the aerodynamic drag of a given hailstone. Knowledge of thunderstorm vertical wind profiles also aides in understanding how varying wind characteristics will impact the damage potential of a given hail event. Although fall speeds exceeding terminal velocities have not been documented in historical literature, the presence of strong thunderstorm downdrafts may contribute to fall velocities which could exceed these values especially within the narrow wind swath associated with the rear-flank downdraft of supercell thunderstorms. However, it is noted that this region is not where the largest hail sizes are typically found. It is currently unknown how the secondary influence from the hardness property of hailstones will alter damage curves. It is possible that damage states could be more severe for smaller size stones embedded within a high wind environment, resulting in damage that may exceed a specific product rating that incorporates only an impact velocity based on purely the diameter and mass. This information will help improve laboratory test methodologies allowing for more accurate and detailed damage curves.

6.3 Compressive Stress

A comparison of the field and laboratory hailstone compressive stress data is provided in Figure 23, and includes field data from 2012 (black diamonds), and from 2013 (black circles outlined in green). In-situ data collected during the 2012 and 2013 field studies have supported qualitative observations reported in historical literature regarding hard and soft hailstones. The impact mechanics of a given hailstone on a material surface are primarily dependent on the kinetic energy of the stone and how that energy is transferred to the material surface to produce damage. The deformation of the falling object or hailstone at the point of impact will lessen the force applied to the impacted material and also will determine the effective duration of impact. The measured compressive force required to fracture a stone is hypothesized to be related to the amount of deformation of the stone and thus the duration of impact. Thus given an equal diameter, mass, and velocity, a stone with a larger peak compressive force would effectively impart a greater force to the impacted material and have the ability to cause more damage. However, laboratory hailstones often fracture on impact along preexisting micro-fractures as a

result of the manufacturing and freezing processes. Therefore improved laboratory methods for producing more consistent hailstones are needed.

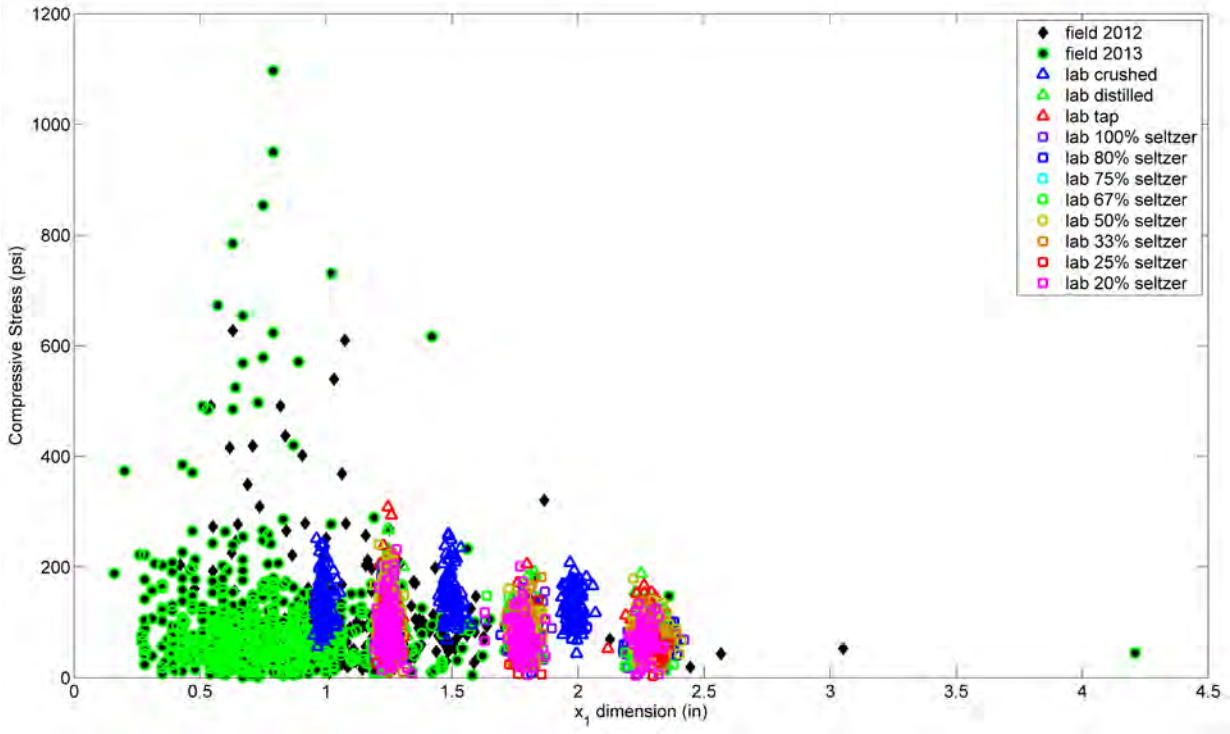


Figure 23: Comparison of field and laboratory compressive force values as a function of the measured x_1 dimension. These data represent all field and lab data collected to date.

The data show there is large variability in the range of compressive stresses for each type of laboratory hailstone, as well as in the field data. The bulk of the field observations and laboratory stones are more clustered at the lower compressive stress values. Some of the variability may be random in nature, but some may be due to inherent flaws in the structure of the hailstones. In the laboratory stones, these flaws may exist because of the conditions in which they are manufactured and extracted. Molds are filled at room temperature and pressure, frozen in temperature-controlled freezers. The stones are extracted at room temperature. These conditions differ from the atmospheric conditions in typical thunderstorms. The range of variations in the field hailstone values may be due to the growth trajectories and number of cycles through the parent thunderstorm updraft.

To better compare these data, the maximum, mean, and minimum compressive stresses were plotted for binned groups of the individual laboratory datasets and the combined 2012 and 2013 field dataset in Figure 24. The bin sizes were selected at 0.25 in. intervals. The values plotted in Figure 24 represent the mean diameter of the stones within the ranges of the given bin. From this figure, it is apparent that the mean compressive stresses of the field data are generally similar to, or slightly higher than those of the seltzer ratio mixtures. The mean compressive stress of the crushed ice laboratory stones is always higher than the field values, independent of the maximum diameter of the stone. This method may provide an

opportunity to investigate the upper bound of compressive stress values observed in the field. Generally, there is little statistical difference between the various mixtures of liquid water and all ratios fall within ±1 standard deviation of the field observations. The relatively good agreement between the laboratory and field data is encouraging, particularly for the smaller diameter hailstones, where there is more confidence in the field data. Good agreement also is depicted for the larger sizes, but until more field data of larger sizes is collected, there is less confidence in the agreement.

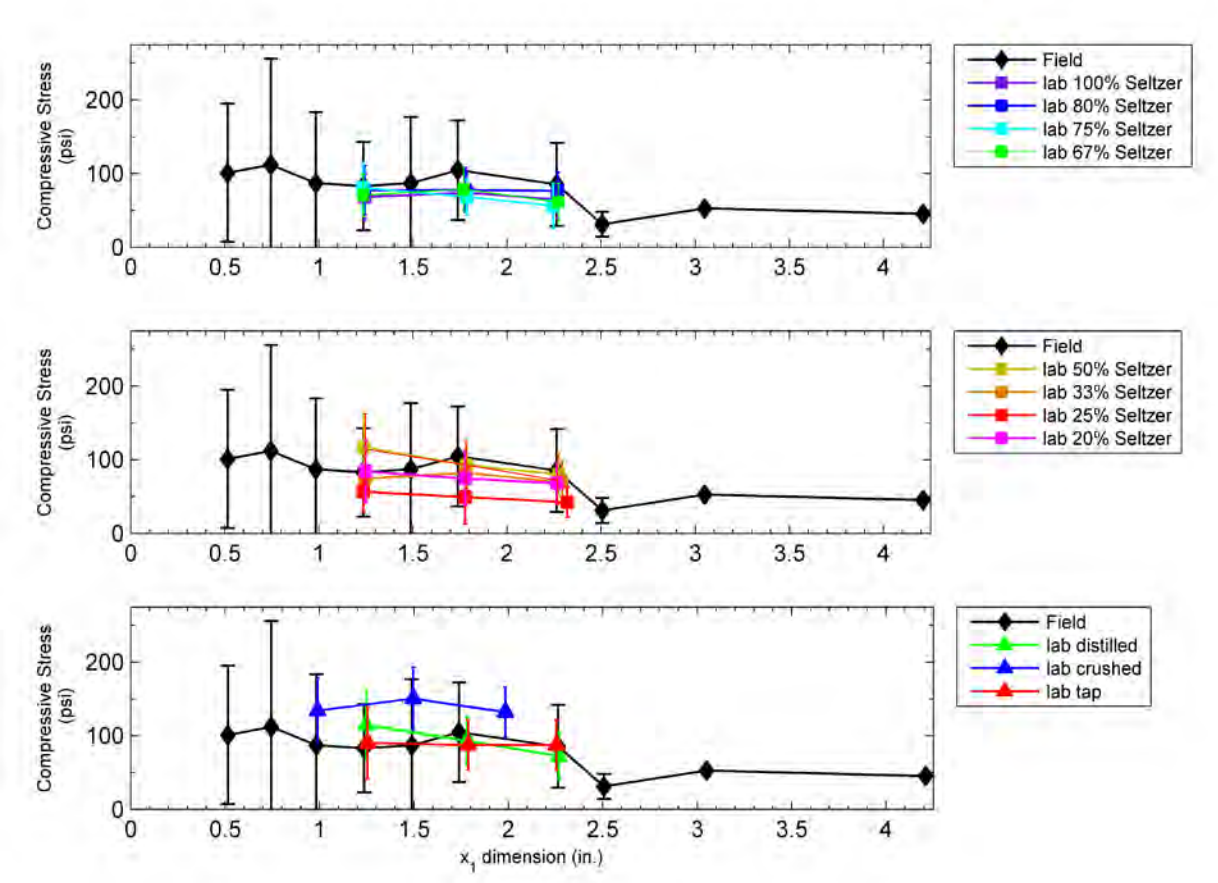


Figure 24: Comparison of the ranges and mean compressive stress data for the combined 2012 and 2013 field data and the various laboratory experimental data. Error bars represent ± 1 standard deviation for each hail size bin. It is noted that for sizes less than 3 in., there are only single data points for field measured stones.

7 Summary

The comparison between laboratory and natural hailstones is yielding interesting results. The relationship between mass and diameter suggests that the kinetic energy of laboratory stones is higher than stones of a similar diameter observed in the field. This is a result of the varying shapes observed in the field and their associated mass and diameter curves versus pure spheres used in the lab. For laboratory impact testing, the use of propulsion speeds derived from terminal velocity estimates of natural hailstones or assuming a perfect sphere would yield a higher kinetic energy than a natural stone

falling at the same velocity. It is intuitive that larger, more massive stones will produce more damage through increased kinetic energy. It also is understood that standardized laboratory test methodologies for hail impacts such as UL 2218 (2012) and FM 4473 (2005) are not truly representative of natural hail impacts; however, in-situ damage observations and damage produced in laboratory experiments coupled with observations of natural hail characteristics suggest that they may be even more conservative than previously thought. The contribution of the hardness property of hailstones and how it relates to the imparted force and impact duration is not as well understood. Future work will continue to focus on understanding this contribution. It is also critical to evaluate how materials (e.g. shingles) perform following prolonged environmental exposure and to effectively evaluate return periods of hail events to provide guidance in selecting appropriate materials.

IBHS will continue work to determine relationships between hardness and other hailstone characteristics, and evaluate environmental characteristics data to determine relationships between weather conditions and the types of hailstones produced. The field hailstone database will continue to provide feedback into the laboratory production of hailstones. The Institute will use the Camera Probe data to examine the distribution and duration of severe hailfall events, and impact angles at each deployment location. Imagery collected from the probe for the single case presented in this report allowed for a crude time-to-space analysis of the hailfall characteristics. It highlighted the ability of rapidly-deployable platforms to provide crucial information on the spatial and temporal characteristics of hail within a thunderstorm, which will help improve modeling applications in which an accurate representation of hailfall is needed.

Although the number of samples collected in 2013 was more than twice that of 2012, the sample sizes are miniscule when compared to the total number of hailstones that fall in a given storm's lifetime. This reinforces the need for continued efforts to collect larger sample sizes from each storm, as well as a larger number of storms. The effectiveness of having two measurement teams was demonstrated by the increased number of high spatial resolution datasets. Even though attempts were made to select parent thunderstorms which were likely to produce the largest hail sizes in the region, there is still very little field data on these larger stones. The data illustrate the relatively rare nature of hailstones larger than 1.5 in. in diameter in these storms.

With new experiences provided this year, the Institute will continue to adapt instrumentation, software, and experimental plans to improve them for use in 2014, and for distribution to additional researchers and partners. IBHS researchers also will explore new instrumentation possibilities to effectively, and non-destructively measure hailstone volumes to improve density calculations. The design of the prototype Camera Probe will be re-evaluated and changes made to make it more functional, rugged, and easily-deployable.

8 References

Beattie, A.G. (1979). Measurements of the kinematics of natural hailstones near ground. *Quarterly Journal of the Royal Meteorological Society*, 105**,** 453-459.

Brown, T.M., Giammanco, I.M., Robinett, D.S. (2012). Observations of hailstone characteristics utilizing a new instrumentation platform. *26th Conference on Severe Local Storms,* Nashville, TN.

Browning, K.A., Ludlum, F.H., Macklin, W.C. (1963). The density and structure of hailstones. *Quarterly Journal of the Royal Meteorological Society,* 89, 75-84.

Browning, K. A., (1964). Airflow and precipitation trajectories within severe local storms which travel to the right of the winds. *Journal of the Atmospheric Sciences,* 21**,** 634–639.

Changnon Jr., S.A. (1973). Hail-sensing and small-scale variability of windblown hail. *Journal of Weather Modification,* 5, 30-42.

Dennis, A.S., Smith Jr., P.L., Peterson, G.A.P., McNeil, R.D. (1971). Hailstone size distributions and equivalent radar reflectivity factors computed from hailstone momentum records. *Journal of Applied Meteorology*, 10, 79–85.

Dowell, D. C., Bluestein, H.B. (1997). The Arcadia, Oklahoma, storm of May 1981: Analysis of a supercell during tornadogenesis. *Monthly Weather Review*, 125, 2562–2582.

Edwards, R., Thompson, R.L. (1998). Nationwide comparisons of hail size with WSR-88D vertically integrated liquid water and derived thermodynamic sounding data. *Weather and Forecasting*, 13, 277-285.

FM Approvals. (2005). *Specificantion test standard for impact resistance testing of rigid roofing materials by impacting with freezer ice balls* (FM 4473). West Glocester, RI: FM Approvals.

FM Approvals. (2010). *Approval standard for single-ply, polymer-modified bitumen sheet, built-up room (BUR) and liquid applied roof assemblies for use in Class 1 and noncombustible roof deck construction* (FM 4470). West Glocester, RI: FM Approvals.

Giammanco, I.M., Brown, T.M. (2013). *Characteristics of Severe Hail 2012 Pilot Field Study: Data Analysis Summary* (IBHS-RC03-2013). Tampa, FL: IBHS.

Gunter, W.S., Schroeder, J.L. (2013). High resolution full-scale measurements of thunderstorm winds. *12th Americas Conference on Wind Engineering*, Seattle, WA.

Heymsfield, A. J., Westbrook, C.D. (2010). Advances in the estimation of ice particle fall speeds using laboratory and field measurements. *Journal of Atmospheric Sciences*, 67, 2469–2482.

Hirth, B.D., Schroeder, J.L., Weiss, C.C. (2008). Surface analysis of the rear-flank downdraft outflow in two tornadic supercells. *Monthly Weather Review*, 136, 2344-2363.

Knight, N. C., Heymsfield, A.J. (1983). Measurement and interpretation of hailstone density and terminal velocity. *Journal of the Atmospheric Sciences*, 40, 1510–1516.

Knight, C. A., Knupp, K.R. (1986). Precipitation growth trajectories in a CCOPE storm. *Journal of the Atmospheric Sciences,* 43, 1057–1073.

Khvorostanov, V.I., Curry, J.A. (2005). Fall velocities of hydrometeors in the atmosphere: Refinements to a continuous analytical power law. *Journal of the Atmospheric Sciences,* 62, 4343-4356.

Kumjian, M.R., Rhzykov, A.V. (2008). Polarimetric signatures in supercell thunderstorms. *Journal of Applied Meteorology,* 47, 1940-1960.

Lakshmanan, V., Smith, T., Stumpf, G., Hondl, K. (2007). The Warning Decision Support System - Integrated Information. *Weather and Forecasting*, 22, 596-612.

Lally, V.E., Leviton, R. (1958). Accuracy of wind determination from the track of a falling object. *Air Force Surveys in Geophysics Report*. Cambridge, MA: Air Force Cambridge Research Center.

Laurie, J.A.P. (1960) Hail and its effects on buildings. *Research Report 176.* Pretoria, South Africa: NBRI.

Lee, B. D., Finley, C.A., Skinner, P.S. (2004). Thermodynamic and kinematic analysis of multiple RFD surges for the 24 June 2003 Manchester, SD cyclic tornadic supercell during Project ANSWERS 2003. *22nd Conference on Severe Local Storms*, Hyannis, MA.

Lee, B.D., Finley, C.A., Karstens, C.D. (2012). The Bowdle, South Dakota, cyclic tornadic supercell of 22 May 2010: Surface analysis of rear-flank downdraft evolution and multiple internal surges. *Monthly Weather Review,* 140, 3419-3441.

Lemon, L.R., Doswell III, C.A. (1979). Severe thunderstorm evolution and mesocyclone structure as related to tornadogenesis. *Monthly Weather Review*, 107, 1184-1197.

Lozowski, E.P., G.S. Strong (1978). Further reflections on the calibration of hailpads. *Atmosphere Ocean*, 16**,** 69-80.

Markowski, P. M., (2002). Hook echoes and rear-flank downdrafts: A review. *Monthly Weather Review*, 130, 852–876.

Matson, R.J., Huggins, A.W. (1980). The direct measurement of the sizes, shapes, and kinematics of falling hailstones. *Journal of the Atmospheric Sciences,* 37, 1107-1125.

Roos, D.v.d.S., Carte, A.E. (1973). The falling behaviour of oblate and spiky hailstones. *J. Recherches Atmospheriques*, 7, 39-52.

Shabbott, C.J., Markowski, P.M. (2006). Surface in-situ observations within the outflow of forward-flank downdrafts of supercell thunderstorms. *Monthly Weather Review*, 134, 1422-1441.

Skinner, P.S., Weiss, C.C., Schroeder, J.L., Wicker, L.J., Biggerstaff, M.I. (2011). Observations of the surface boundary structure within the 23 May 2007 Perryton, Texas supercell. *Monthly Weather Review*, 139, 3730-3749.

Stumpf, G.J., Smith, T.M., Gerard, A.E. (2002). The Multiple-Radar Severe Storm Analysis Program (MR-SSAP) For WDSS-II. *21st Conf. on Severe Local Storms*, San Antonio, TX.

Underwriters Laboratory. (2012). *UL 2218: Standard for impact resistance of prepared roof covering materials.* Northbrook, IL: UL.

Van Den Broeke, M. S., Straka, J.M., Rasmussen, E.N. (2008). Polarimetric radar observations at low levels during tornado life cycles in a small sample of classic southern plains supercells. *Journal of Applied Meteorology and Climatology*, 47, 1232–1247.

Witt, A., Eilts, M.D., Stumpf, G.J., Johnson, J.T., Mitchell, E.D., Thomas, K.W. (1998). An enhanced hail detection algorithm for the WSR-88D. *Weather and Forecasting*, 13, 286–303.